Structural and Multidisciplinary Optimization (2024) 67:217
https://doi.org/10.1007/s00158-024-03938-0

RESEARCH PAPER

# Topology optimization for particle trajectory control considering particle-rigid wall contact

Young Hun Choi[1] · Gil Ho Yoon[1]

Received: 10 June 2024 / Revised: 1 October 2024 / Accepted: 18 November 2024 / Published online: 19 December 2024


## Abstract

This research develops a new topology optimization scheme for controlling the trajectory of particles considering contacts between particles and structure. Existing density-based topology optimization schemes struggle with accounting for particle-rigid wall contact because of the discontinuous behavior and the non-smooth shape of topological design. To solve these challenging issues, this research introduces a new particle-rigid wall contact model and its application method for topology optimization. In addition, new constraints to manipulate the trajectories of a particle enabling it to pass through or avoid a specific point are developed. The sensitivity of an objective function related to the particle trajectory is derived by the adjoint approach. Several optimization examples are considered to demonstrate the ability to control the particle trajectories while accounting for the phenomena of the particle-rigid wall contact.

**Keywords** Topology optimization · Particle-rigid wall contact · Particle analysis · Particle collision

## 1 Introduction

The aim of this study is to present a new topology optimization for controlling particle trajectories, especially considering particle-rigid wall interactions, as shown in Fig. 1. Density-based topology optimization encounters difficulties in accounting for contacts between particles and rigid walls. These challenges arise due to the discontinuous properties of contacts and the non-smooth contours resulting from topology optimization. To address these challenges, this study presents a model that utilizes the concept of springs with high stiffness for particle-rigid wall interaction. To incorporate this model into the topology optimization, the topological design is converted into a smooth rigid wall by mapping design variables to smooth and spatially continuous variables. The sensitivities of objective functions related to particle motions are analytically derived using an adjoint approach. Additionally, to effectively manage particle trajectories, a constraint allowing particles to pass through or circumvent a designated point is introduced. Based on the above, a method for incorporating particle-rigid wall interactions into topology optimization is studied.

Particle contact has been an area of extensive research. Various experimental studies have focused on the phenomenon of particle contact (Sommerfeld and Huber 1999; Joseph et al. 2001; Ardekani and Rangel 2008; Ardekani et al. 2009; Sommerfeld 2003; Wang et al. 2020; O'Regan et al. 2023). In Sommerfeld and Huber (1999), collisions between particles and various kinds of wall were experimentally investigated. Moreover, particle-wall collisions have been studied across various types of fluids, including viscous fluids (Joseph et al. 2001; Ardekani and Rangel 2008), viscoelastic fluids (Ardekani et al. 2009), and in turbulent flow (Sommerfeld 2003). Recent studies have focused on particle-wall collisions involving particles of various shapes (Wang et al. 2020; O'Regan et al. 2023). Meanwhile, many computational models and simulation methods for the particle-wall collision are studied and developed (Popp 2018; Kildashti et al. 2020; Cheon and Kim 2018; Gui et al. 2016; Craveiro et al. 2021; Campbell et al. 2000; Matuttis and Chen 2014; Meyer and Deglon 2011; Zhu et al. 2008; Paulick et al. 2015). In Popp (2018), a computational method for analyzing contacts between solids and structures utilizing a nonlinear finite element approach is pioneered. In Kildashti et al. (2020), it is introduced a novel model for accurately

Responsible Editor: Makoto Ohsaki

✉ Gil Ho Yoon
ghy@hanyang.ac.kr

[1] Department of Mechanical Engineering, Hanyang University, Seoul 04763, South Korea

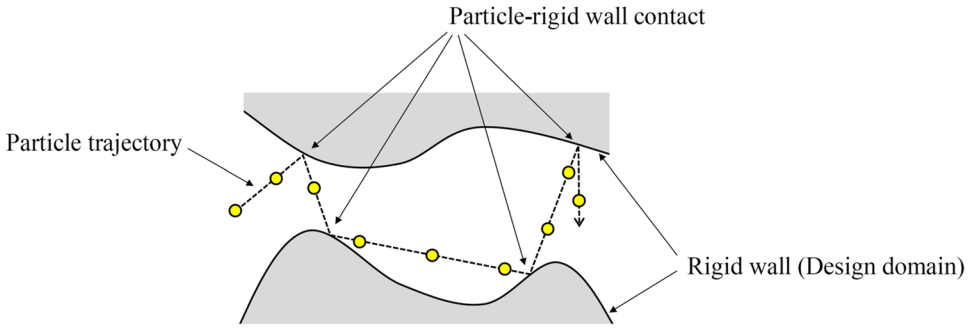


**Fig. 1** Topology optimization of the trajectory of a particle considering contact between the particle and rigid wall

computing contact forces for super-quadric particles. In Gui et al. (2016), a new model for collision of non-spherical particles and rigid wall has been presented. In Craveiro et al. (2021), a new methodology to address contacts among rigid convex particles is developed, while an efficient numerical method to consider particle contact is proposed in Cheon and Kim (2018). Research presented in Campbell et al. (2000) focused on developing an algorithm for managing contacts in smoothed particle hydrodynamics. A popular technique in this field is the Discrete Element Method (DEM). In Matuttis and Chen (2014), detail methods to analyze particle contacts using the DEM are presented. A review of other models for particle collision can be found in Meyer and Deglon (2011). Moreover, in Zhu et al. (2008) and Paulick et al. (2015), review on the use of the DEM for simulating particle contact phenomena is provided. These studies highlight the diversity of methodologies explored in the study of particle contacts.

While numerous studies have delved into optimizations related to simulating the particle contact or using the DEM (O'Shaughnessy et al. 2022; Masoero et al. 2022; Balevičius et al. 2006; Chen et al. 2020), research focusing on the topology optimization that incorporates particle-rigid wall contact remains scarce. For instance, in Balevičius et al. (2006), a size optimization was conducted with considering the particle contact by using the DEM. In Chen et al. (2020), an optimization based on a response surface model obtained by the DEM analysis results was presented. Because the DEM is widely used in various fields including the structural analysis (Tavarez and Plesha 2007) and heat transfer (Peng et al. 2020), methodologies for the structural topology optimization using the DEM was developed in O'Shaughnessy et al. (2022) and Masoero et al. (2022). However, to the best of our knowledge, research that integrates the particle-rigid wall contact with the topology optimization is not explored.

The topology optimization has experienced significant advancements across various fields, initially focusing on structural problems as introduced in Bendsøe and Kikuchi (1988), and later expanding into more complex fluid dynamics. Comprehensive reviews of the field have been documented in Sigmund and Maute (2013) and van Dijk et al. (2013). Following the introduction of fluid topology optimization in Borrvall and Petersson (2003), a various range of methodologies have been developed, addressing turbulent flow (Papoutsis-Kiachagias et al. 2011; Dilgen et al. 2018), fluid–structure interaction (Yoon 2010) and two-phase flow (Deng et al. 2017; Yoon and Kim 2023). A detailed review of previous studies is available in Alexandersen and Andreasen (2020) and Lundgaard et al. (2018). More recently, studies presented in Yoon (2020), Andreasen (2020), Yoon (2022) and Choi and Yoon (2023a) have developed methods for controlling particles suspended in fluid. In Yoon (2020), Andreasen (2020), studies have pioneered topology optimizations aimed at controlling particles suspended in fluids. Additionally, Yoon (2022) focused on optimizing particles suspended in transient fluid. Furthermore, Choi and Yoon (2023a) introduced an educational MATLAB code specifically designed for this purpose. This demonstrates that the considerable progress has made over the years in the field of the topology optimization.

This research focuses on considering the particle-rigid wall contact within the topology optimization. Despite of these advancements in this field, the topology optimization involving particles, especially considering particle-rigid wall contact, has been less explored. In this paper, the topological density is mapped into smooth shaped rigid wall to account for the particle-rigid wall contact in the topology optimization. A simple spring model to compute the contact between particles and rigid wall which is firstly introduced in the author's previous work (Choi and Yoon 2023b) is utilized for topology optimization to manipulate the trajectories of particles. Furthermore, a convenient constraint to effectively control the trajectory of the particle is developed. Although there have been numerous studies on simulating particles and optimization related to particles, the topology optimization for this specific problem remains less developed. This study attempts to solve this problem by incorporating particle-rigid wall contact into the framework of topology optimization.

The remainder of this paper is organized as follows: Sect. 2 introduces a model designed to simulate collisions between particles and rigid wall. Additionally, it discusses the method for transforming topological density into smooth

shaped rigid wall. Subsequently, the sensitivity analysis of arbitrary functions related to particle motion is performed using the adjoint equation, and new constraints are proposed to effectively control particle trajectories. Section 3 presents several numerical examples to demonstrate the possibilities of incorporating particle-rigid wall contact into the topology optimization. In Sect. 4, the conclusion with a summary of the paper and future works are provided.

## 2 A new particle-rigid wall contact for topology optimization

In this section, a new computational framework to simulate the motion of particle considering the collision between particles and rigid wall is developed; the collision phenomena among particles are not considered. In the new computational framework, the effects of the particle collisions are approximated using the contact forces of the springs as illustrated in Fig. 2 and the force exerted on a particle due to its collision to surface is determined using the penetration distance of the particle. In topology optimization framework, the contact surfaces are determined by a continuous scalar function, $\rho(\mathbf{x})$ and a specific criterion ($\rho_{\text{wall}}$). A new transforming process of the design variables to the contact surface is developed too.

### 2.1 Governing equation for particle motion and a new contact force modeling

Newton's second law for particle considering the gravity force as well as the contact force from wall can be written as follows:

$$\frac{\mathrm{d}}{\mathrm{d}t}(m\mathbf{v}) = \mathbf{F}_{\text{gravity}} + \mathbf{F}_{\text{contact}}, \quad \mathbf{v} = \frac{\mathrm{d}\mathbf{x}}{\mathrm{d}t} \tag{1}$$

where the mass and the velocity of particle are denoted by $m$ and $\mathbf{v}$, respectively. In the present research, the contact force in the field of the density is expressed as follows:

$$\mathbf{F}_{\text{contact}} = k\,\delta(\mathbf{x},\rho)\,s(\rho)\,\mathbf{n}(\rho) \tag{2}$$

where the contact stiffness is denoted by $k$ and $\rho$ is a continuous scalar function to obtain an interface curve which will be covered in the next section. The gap in the normal direction between the particle position $\mathbf{x}(t)$ and the contact surface $\mathbf{x}_c$ is denoted by $\delta$ and the normal vector is $\mathbf{n}$. A function, $s(\rho)$, is newly introduced to ensure that the contact force is only exerted when a particle contacts on rigid wall structure. The new function for $s(\rho)$ is defined with the $S$-shaped sigmoid function and the unit step function. Note that all the components of the contact force are related to the spatial density of the topology optimization $\rho$.

In the present research, the following procedures are developed for computing the contact force in Eq. (2). Firstly, the unit normal vector is derived from the fact that the gradient of $\rho$ is perpendicular to the curve $\rho = C$, where $C$ is a constant. Mathematically, this can be expressed as follows:

$$\mathbf{n} = -\nabla\rho \,/\, \|\nabla\rho\| \tag{3}$$

The distance in the normal direction between the contact surface position, $\mathbf{x}_c$, and the position of the particle, $\mathbf{x}(t)$, is defined using the dot product of vectors, i.e., $\mathbf{x}(t) - \mathbf{x}_c$, and $-\mathbf{n}$ as follows:

$$\delta_{\text{true}} = (\mathbf{x}(t) - \mathbf{x}_c)\cdot(-\mathbf{n}) = \frac{(\mathbf{x}(t) - \mathbf{x}_c)\cdot\nabla\rho}{\|\nabla\rho\|} \tag{4}$$

Assuming that $\mathbf{x}(t)$ is sufficiently close to $\mathbf{x}_c$, the density variables, $\rho$, near the contact surface, i.e., $\rho \approx \rho_{\text{wall}}$, can be approximated using the first-order Taylor expansion. Inserting this equation concerning $\rho$ into Eq. (4) gives the approximate value for $\delta$ as follows:

$$\begin{aligned} \rho &\approx \rho_{\text{wall}} + \frac{\partial\rho}{\partial\mathbf{x}}\cdot(\mathbf{x} - \mathbf{x}_c) \\ \delta &= \frac{\partial\rho}{\partial\mathbf{x}}\cdot\frac{\mathbf{x} - \mathbf{x}_c}{\|\nabla\rho\|} \approx \delta_{\text{approx}} \\ \delta_{\text{approx}} &= \frac{\rho - \rho_{\text{wall}}}{\|\nabla\rho\|} \end{aligned} \tag{5}$$

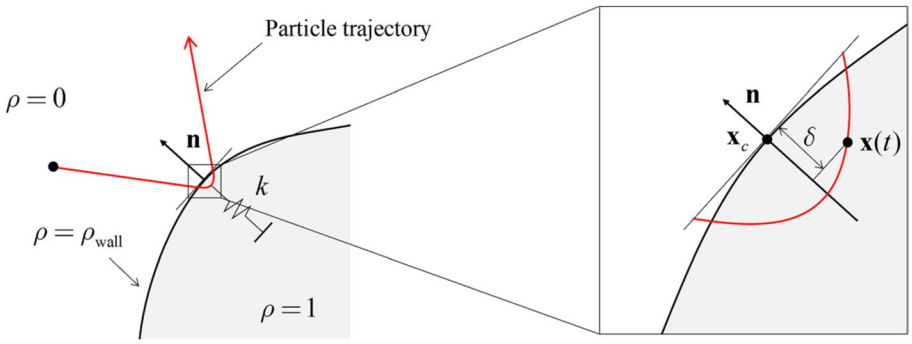


**Fig. 2** A particle-rigid wall contact model utilizing a spring and spatial variable $\rho$

The main reason for this approximation is that using $\delta$ directly requires computing $\mathbf{x}_c$ which is obtained from the implicit equation $\rho(\mathbf{x}_c) = \rho_{\text{wall}}$. In contrast, the approximation can be calculated directly from $\rho$. The approximated contact force can be derived by integrating both Eqs. (3) and (5) into Eq. (2) as follows:

$$\mathbf{F}_{\text{contact}} = k \cdot \frac{\rho_{\text{wall}} - \rho}{\|\nabla\rho\|^2} \cdot \nabla\rho \cdot s(\rho) \tag{6}$$

where the function $s(\rho)$ can be expressed through either $s_{\text{unit}}$ or $s_{S\text{-shape}}$ as detailed in the following equations.

$$\begin{aligned} s_{\text{unit}}(\rho) &= \begin{cases} 1, & \rho \geq \rho_{\text{wall}} \\ 0, & \rho < \rho_{\text{wall}} \end{cases} \\ s_{S\text{-shape}}(\rho) &= \frac{1}{e^{-a(\rho-\rho_{\text{wall}})} + 1} \end{aligned} \tag{7}$$

where $a$ is set to a sufficiently large number, $10^6$, to do not exert the contact force on the particles when they pass through the void region. Note that the above formulation in Eq. (6) with Eq. (7) is one of the new and important contributions in this paper. The determination of a proper envelope of the pseudo rigid wall, $\rho_{\text{wall}}$, should be addressed and the adjoint sensitivity analysis considering Eq. (6) should be developed further.

Figure 3 provides a simplified example to validate the accuracy of the approximated $\delta$ in Eq. (5). To achieve that the curve, $\rho = \rho_{\text{wall}}$, becomes a circle of radius $R$, a surface $(\rho = 1 - 12.5((x-0.5)^2 + (y-0.5)^2))$ is used, as illustrated in Fig. 3a. Figure 3b shows the trajectory of the particle along the blue curve $(y = 13.44(x-0.5)^2 + 0.66, \quad 0.45 \leq x \leq 0.55)$ which is the line where $\delta$ is calculated. The location of a particle is represented by $\mathbf{x}_{\text{particle}} = (x_{\text{particle}}, y_{\text{particle}})$. Figure 3c compares the approximated $\delta$, i.e., $\delta_{\text{approx}}$, with the true value, i.e., $\delta_{\text{true}}$, where the true $\delta$ in this example is computed by Eq. (8).

$$\delta_{\text{true}} = R - \|\mathbf{x}_{\text{particle}} - (0.5, 0.5)\| \tag{8}$$

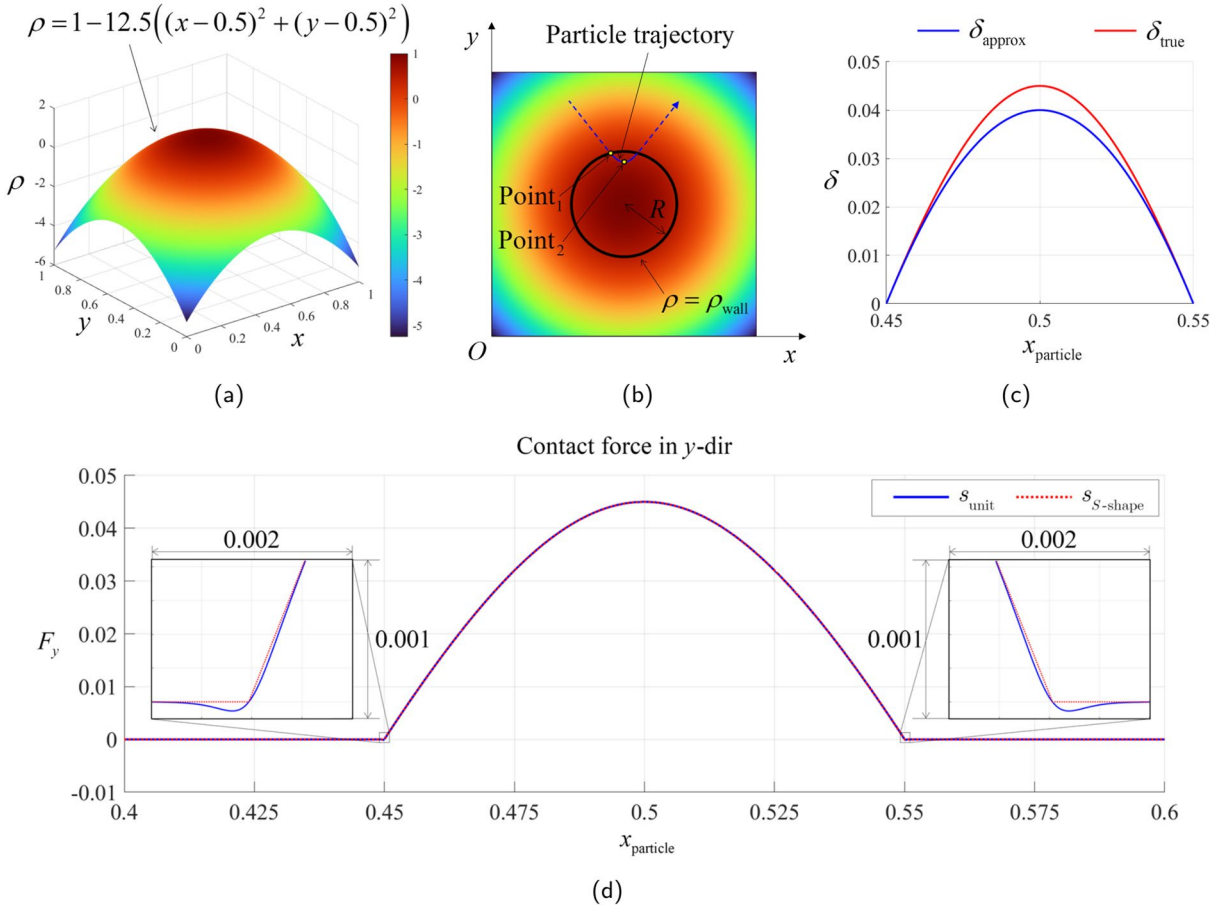


**Fig. 3** A simple example for comparing the approximated $\delta$ with true value. **a** The spatial density function, $\rho$, **b** rigid wall and trajectory of a particle ($\rho_{\text{wall}} = 0.5$, $R = 0.2$, Point$_1$ = (0.45, 0.6936) and Point$_2$ = (0.5, 0.66)), **c** comparison between the approximation and true value of $\delta$ and **d** contact force in $y$-dir ($F_y$)

where $\rho_{\text{wall}}$ and $R$ are set to 0.5 and 0.2, respectively. In Fig. 3b, at $\text{Point}_1$ (0.45, 0.6936), the particle penetrates the rigid wall, while at $\text{Point}_2$ (0.5, 0.66), the largest discrepancy between $\delta_{\text{approx}}$ and $\delta_{\text{true}}$ is observed. Figure 3d shows the difference in the forces with $s_{\text{unit}}$ and $s_{S\text{-shape}}$. When $s_{\text{unit}}$ is used, particles do not experience the contact forces from the outside. In contrast, with $s_{S\text{-shape}}$, the contact forces exist even if particles are outside the structure and this force is an attraction force. The numerical examples presented in this paper adopt a high value for $k$ to minimize penetration, ensuring a physically reasonable solution.

## 2.2 Deriving smooth shaped interface curve from the topological density

This section provides a method to derives the smooth shaped interface curve that refers to a curve which is smooth enough that there are no sharp bends and corners. To calculate the motion of particles with the present scheme, obtaining a smooth shaped interface curve is necessary. However, in the density-based topology optimization, the use of a structured mesh results in boundaries that are not smooth. To address this problem, an explicit smooth curve is generated by using the spatial density function, $\rho(\mathbf{x})$.

Figure 4 highlights how to obtain the spatial density function, $\rho(\mathbf{x})$, used in the above developed formula where the element-wise spatial density values, $\gamma$, are the design variables. Note that it is not necessary to use element-wise design variables, as node-wise variables can also be used. However, since many previous topology optimization studies adopt the element-wise approach, this study uses element-wise design variables for future integration with other fields (such as structural, fluid). To derive the smooth shaped interface curve which is crucial for the computing the contact force, the nodal variables are computed by averaging or interpolating the density values of the elements which has the corresponding node of interest. To obtain the spatial density function, $\rho(\mathbf{x})$, the nodal density is calculated by using Eq. (9) through Eq. (16). With the nodal density values, $\boldsymbol{\rho}$, the spatial density function, $\rho(\mathbf{x})$, is defined using the shape function of the nine-node quadrilateral element, $\mathbf{N}(\mathbf{x})$, as shown in Fig. 4. With the criterion $\rho_{\text{wall}}$, the smooth curve defining wall can be obtained as shown in Fig. 4.

To obtain the smooth shaped interface curve, the following process is presented. First, the design variables are filtered using a radius $r_{\text{min}}^{(1)}$ to impose a minimum length scale.

$$\begin{aligned} \bar{\gamma}_i &= \sum_{j=1}^{\text{NE}} w_{ij}^{(1)} \gamma_j \Big/ \sum_{j=1}^{\text{NE}} w_{ij}^{(1)}, \\ w_{ij}^{(1)} &= \max\left(0,\, r_{\text{min}}^{(1)} - \text{dist}(i,j)\right) \end{aligned} \tag{9}$$

where $\gamma_i$ represents the design variable, the subscript $i$ ranges from 1 to NE , and $\bar{\gamma}$ is the density filtered variable. The term $w_{ij}^{(k)}$ is defined as $\max(0,\, r_{\text{min}}^{(k)} - \text{dist}(i,j))$, where $\text{dist}(i,j)$ is

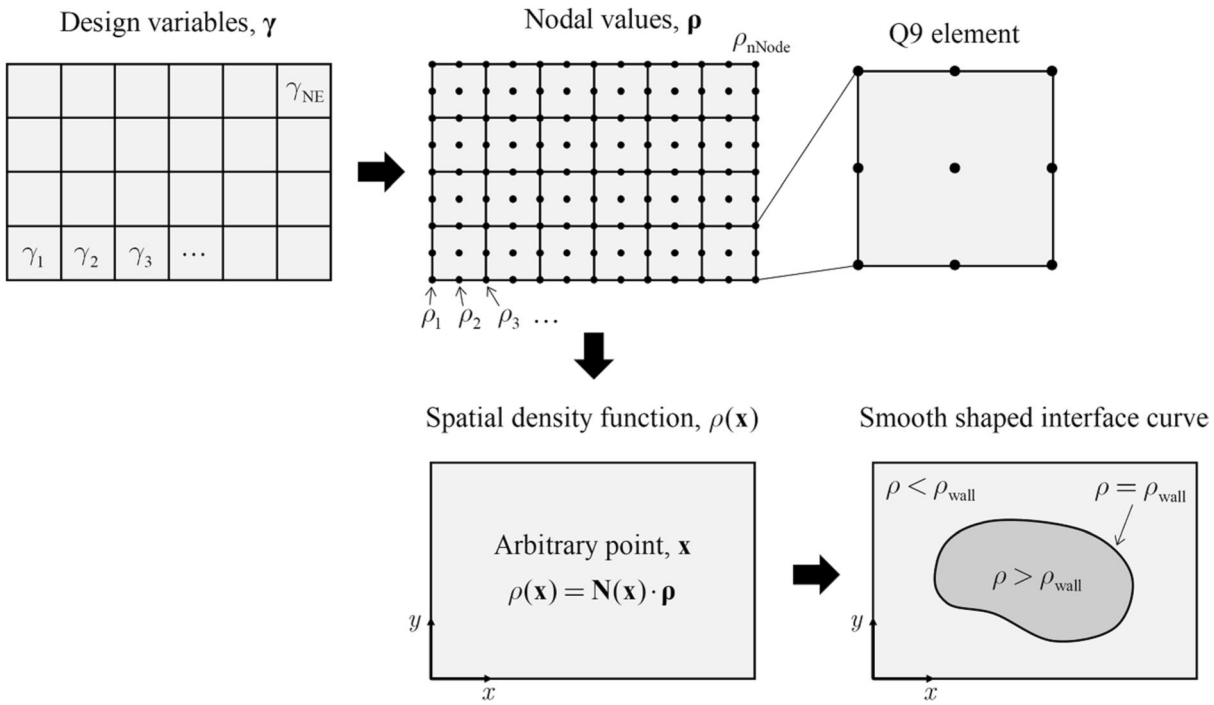


**Fig. 4** Procedure obtaining the smooth shaped interface curve of the rigid wall and the continuous topological density $\rho$ from the element topological density $\gamma$ (the number of elements: NE, the number of nodes: nNode)

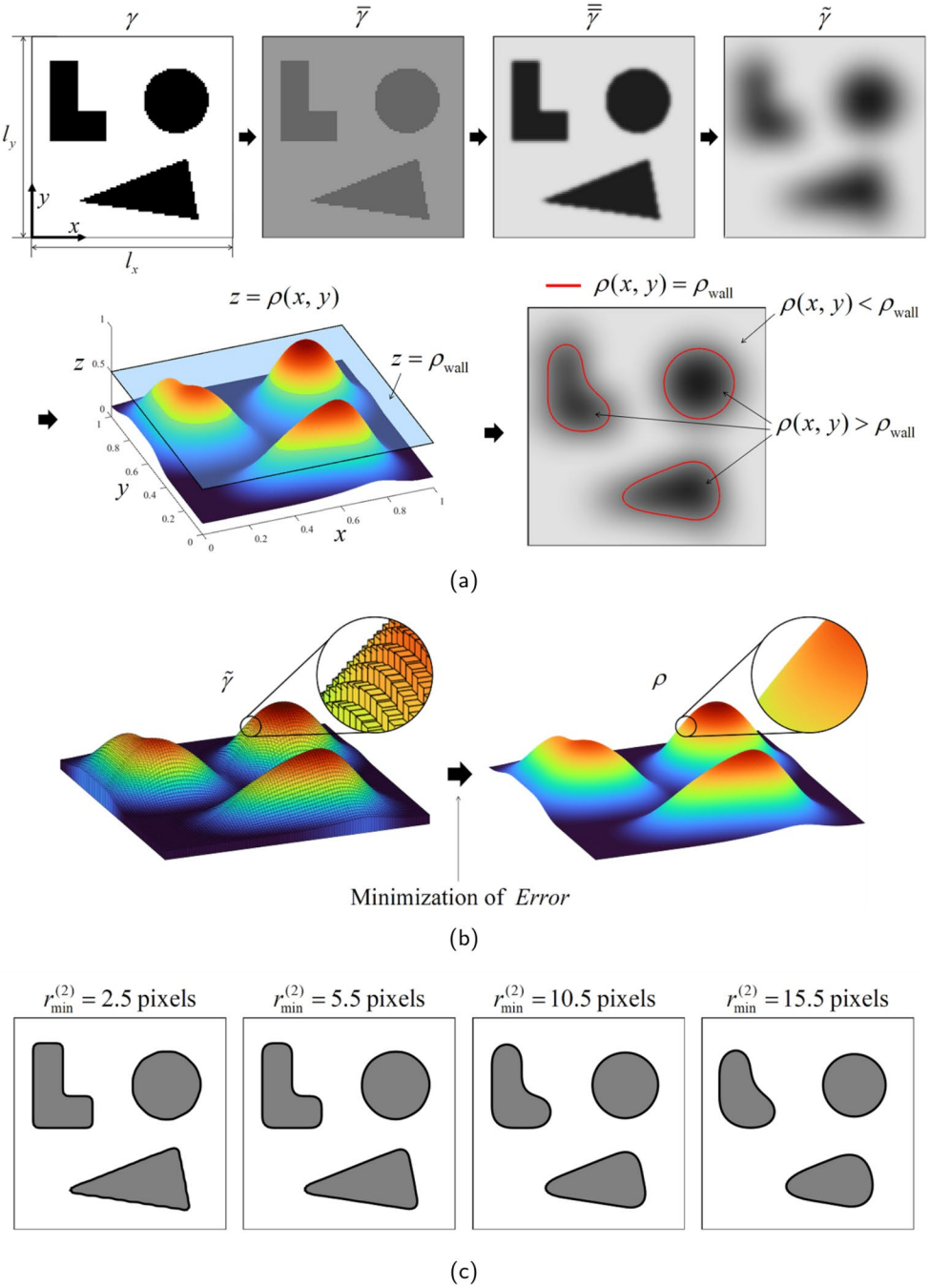


**Fig. 5** An example obtaining the continuous topological density $\rho$ and the interface curve of the solid. **a** The detail procedure ($l_x = 1$, $l_y = 1$, $\rho_{\text{wall}} = 0.5$, $\rho_{\Delta} = 0.1$, $r_{\text{min}}^{(1)} = 2.5$ pixels and $r_{\text{min}}^{(2)} = 15.5$ pixels), **b** the transformation of the density from $\tilde{\boldsymbol{\gamma}}$ to $\rho$ and **c** the smooth rigid wall with the different radii of the density filtering ($r_{\text{min}}^{(2)} = 2.5$, 5.5, 10.5 and 15.5 pixels)

the distance between $i$-th and $j$-th elements. After the density filtering, an $S$-shape function is applied, which is a common procedure in topology optimization to ensure a minimum length scale of the structure as discussed in previous studies (Zhou et al. 2015; Choi and Yoon 2024). A new variable $\bar{\bar{\gamma}}$ is then defined by Eq. (10).

$$\bar{\bar{\gamma}}_i = S\left(\bar{\gamma}_i\right) \tag{10}$$

where $S(x)$ denotes the $S$-shape sigmoid function. The $S$-shape sigmoid function with parameters $\alpha$ for defining the slope and $\beta$ for defining the shift is firstly introduced to topology optimization in Yoon and Kim (2003) and as follows:

$$S(x) = \frac{1}{e^{\alpha(x-\beta)} + 1} \tag{11}$$

where $\alpha$ and $\beta$ are set to $-4$ and 0.5, respectively. As $\bar{\bar{\gamma}}$ is obtained by using the $S$-shape sigmoid function, the values of $\bar{\bar{\gamma}}$ at the boundary of the solid change abruptly. Since the gradient is needed for calculating the contact force in Eq. (6), the following smoothing is additionally applied and a new smoothed variables $\tilde{\gamma}$ is derived using the following filtering with a radius $r_{\min}^{(2)}$.

$$\begin{aligned} \tilde{\gamma}_i &= \sum_{j=1}^{\mathrm{NE}} w_{ij}^{(2)} \bar{\bar{\gamma}}_j \Big/ \sum_{j=1}^{\mathrm{NE}} w_{ij}^{(2)}, \\ w_{ij}^{(2)} &= \max\left(0, r_{\min}^{(2)} - \mathrm{dist}(i,j)\right) \end{aligned} \tag{12}$$

Note that the two steps can be combined by appropriately adjusting the parameters. However, in this paper, the parameters related to the minimum length scale and smoothness are utilized separately, providing more flexibility in controlling both aspects independently.

After obtaining the smoothed variables, the densities of the elements are mapped to nodal densities which are set to minimize a squared difference between the element densities and the nodal densities. This can be formulated as a form of the optimization problem as follows:

$$\min_{\boldsymbol{\rho}} \ \mathit{Error} = \sum_{e=1}^{\mathrm{NE}} \int_{\Omega_e} \left(\rho(\mathbf{x}) - \tilde{\gamma}_e\right)^2 \mathrm{d}\Omega, \tag{13}$$

where *Error* is the squared difference, $\boldsymbol{\rho}$ is the nodal density vector, $\rho(\mathbf{x})$ is the spatial density, $\tilde{\gamma}_e$ is the smoothed density of $e$-th element and $\Omega_e$ is the domain of the $e$-th element. The squared difference, *Error*, and its derivative with respect to the nodal densities are obtained as follows:

$$\begin{aligned} \mathit{Error} &= \boldsymbol{\rho}^{\mathrm{T}}\mathbf{M}\boldsymbol{\rho} - \boldsymbol{\rho}^{\mathrm{T}}\mathbf{Q}\tilde{\boldsymbol{\gamma}} + \sum_{e=1}^{\mathrm{NE}} \int_{\Omega_e} \left(\tilde{\gamma}_e^2\right) \mathrm{d}\Omega, \\ \frac{\partial}{\partial \boldsymbol{\rho}} \mathit{Error} &= \mathbf{M}\boldsymbol{\rho} - \mathbf{Q}\tilde{\boldsymbol{\gamma}}, \end{aligned} \tag{14}$$

where $\tilde{\boldsymbol{\gamma}}$ is the vector of the smoothed densities of the elements. $\mathbf{M}$ and $\mathbf{Q}$ are defined as follows:

$$\begin{aligned} \mathbf{M} &= \sum_{e=1}^{\mathrm{NE}} \left( \int_{\Omega_e} \mathbf{N}_e^{\mathrm{T}} \mathbf{N}_e \, \mathrm{d}\Omega \right), \\ \mathbf{Q} &= \left[ \mathbf{Q}_1 \ \mathbf{Q}_2 \ \cdots \ \mathbf{Q}_{\mathrm{NE}} \right], \\ \mathbf{Q}_e &= \int_{\Omega_e} \mathbf{N}_e^{\mathrm{T}} \, \mathrm{d}\Omega, \end{aligned} \tag{15}$$

where $\mathbf{N}_e$ is the shape function of $e$th element. In this paper, the second order elements consisting of 9 nodes are used. The nodal density is set to the value that satisfies the condition that the derivative should be zero (i.e. $\boldsymbol{\rho} = \mathbf{M}^{-1}\mathbf{Q}\tilde{\boldsymbol{\gamma}}$). Then, by multiplying the shape function to the nodal densities $\boldsymbol{\rho}$, the spatial density $\rho(\mathbf{x})$ can be obtained by follows:

$$\rho(\mathbf{x}) = \mathbf{N}(\mathbf{x})\,\mathbf{M}^{-1}\mathbf{Q}\,\tilde{\boldsymbol{\gamma}} \tag{16}$$

where $\mathbf{N}(\mathbf{x})$ represents the global shape function at position $\mathbf{x}$. The dimensions of each component on the right-hand side are as follows: $1 \times n_{\mathrm{Node}}$, $n_{\mathrm{Node}} \times n_{\mathrm{Node}}$, $n_{\mathrm{Node}} \times \mathrm{NE}$ and $\mathrm{NE} \times 1$ where $n_{\mathrm{Node}}$ refers to the number of nodes. Subsequently, using the above equation, the smooth curve defining the wall can be obtained. This curve is defined as the set of $\mathbf{x}$ such that the spatial density $\rho(\mathbf{x})$ is equal to the constant $\rho_{\mathrm{wall}}$. The above process is derived from minimizing the error between element-wise and nodal design variables. However, alternative approaches can also be employed. For instance, a method based on PDE filtering can be utilized as discussed in Appendix 1.

An example of the above process is expressed in Fig. 5. The process of converting the design variable, $\gamma$, to the spatial density, $\rho$, is detailed in Fig. 5a. In this process, the design is smoothed and transformed into the final red outline. In Fig. 5b, the smoothed density, $\tilde{\gamma}$, is converted into the continuous spatial density, $\rho$, using the minimization problem formulated in Eq. (13). The amount of smoothing can be controlled by the radius of the density filtering, $r_{\min}^{(2)}$, as shown in Fig. 5c.

## 2.3 Sensitivity analysis with particle-rigid wall contact

To compute the sensitivity of an arbitrary function $c$ composed of the position, velocity, and acceleration of the particle, the Lagrangian $L$ is defined as follows:

$$L = \int_0^{t_f} c(\mathbf{x}, \dot{\mathbf{x}}, \ddot{\mathbf{x}}) \, \mathrm{d}t + \int_0^{t_f} \lambda^{\mathrm{T}}(m\ddot{\mathbf{x}} - \mathbf{F}) \, \mathrm{d}t, \tag{17}$$

where the Lagrange multiplier is denoted by $\lambda$. Differentiating this equation yields the following.

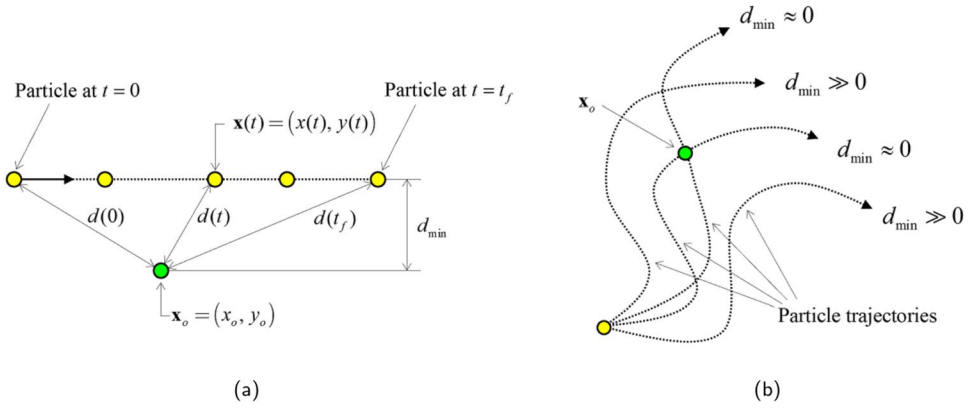


**Fig. 6** The distance between the particle trajectory and the target point $\mathbf{x}_o$. **a** The distance between the position of particle at each time and the target point $\mathbf{x}_o$ and **b** the minimum distances for different particle trajectories

$$\begin{aligned}\frac{\mathrm{d}L}{\mathrm{d}\gamma_e} &= \int_0^{t_f} \left( \frac{\mathrm{d}}{\mathrm{d}\gamma_e} c(\mathbf{x}, \dot{\mathbf{x}}, \ddot{\mathbf{x}}) + \lambda^{\mathrm{T}} \frac{\mathrm{d}}{\mathrm{d}\gamma_e} (m\ddot{\mathbf{x}} - \mathbf{F}) \right) \mathrm{d}t \\ &= \int_0^{t_f} \left( \frac{\partial c}{\partial \mathbf{x}} \frac{\mathrm{d}\mathbf{x}}{\mathrm{d}\gamma_e} + \frac{\partial c}{\partial \dot{\mathbf{x}}} \frac{\mathrm{d}\dot{\mathbf{x}}}{\mathrm{d}\gamma_e} + \frac{\partial c}{\partial \ddot{\mathbf{x}}} \frac{\mathrm{d}\ddot{\mathbf{x}}}{\mathrm{d}\gamma_e} \right) \mathrm{d}t, \\ &\quad + \int_0^{t_f} \left( m\lambda^{\mathrm{T}} \frac{\mathrm{d}\ddot{\mathbf{x}}}{\mathrm{d}\gamma_e} - \lambda^{\mathrm{T}} \frac{\mathrm{d}\mathbf{F}}{\mathrm{d}\gamma_e} \right) \mathrm{d}t,\end{aligned} \tag{18}$$

where the design variable of the $e$th element is denoted by $\gamma_e$. Note that the function $c$ is only dependent on the position, velocity and acceleration of the particle. Using the chain rule, the function $c$ is differentiated as the sum of three terms: the derivatives of $c$ with respect to the position, velocity, and acceleration and the product of the derivative of each variable with respect to the design variable. The derivative of the force from mainly formulated with the contact force along the contact surface acting on the particle, $\mathbf{F}$, can be computed as:

$$\frac{\mathrm{d}\mathbf{F}}{\mathrm{d}\gamma_e} = \frac{\partial \mathbf{F}}{\partial \mathbf{x}} \frac{\mathrm{d}\mathbf{x}}{\mathrm{d}\gamma_e} + \frac{\partial \mathbf{F}}{\partial \gamma_e} \tag{19}$$

Substituting the above equation into Eq. (18) and applying the integration by parts result in the following equation.

$$\begin{aligned}\frac{\mathrm{d}L}{\mathrm{d}\gamma_e} &= \left[ \left( \frac{\partial c}{\partial \dot{\mathbf{x}}} - \frac{\mathrm{d}}{\mathrm{d}t} \left( \frac{\partial c}{\partial \ddot{\mathbf{x}}} \right) - m\dot{\lambda}^{\mathrm{T}} \right) \frac{\mathrm{d}\mathbf{x}}{\mathrm{d}\gamma_e} + \left( \frac{\partial c}{\partial \ddot{\mathbf{x}}} + m\lambda^{\mathrm{T}} \right) \frac{\mathrm{d}\dot{\mathbf{x}}}{\mathrm{d}\gamma_e} \right]_0^{t_f} \\ &\quad + \int_0^{t_f} \left( \frac{\partial c}{\partial \mathbf{x}} - \frac{\mathrm{d}}{\mathrm{d}t} \left( \frac{\partial c}{\partial \dot{\mathbf{x}}} \right) + \frac{d^2}{dt^2} \left( \frac{\partial c}{\partial \ddot{\mathbf{x}}} \right) - \lambda^{\mathrm{T}} \frac{\partial \mathbf{F}}{\partial \mathbf{x}} + m\ddot{\lambda}^{\mathrm{T}} \right) \frac{\mathrm{d}\mathbf{x}}{\mathrm{d}\gamma_e} \, \mathrm{d}t \\ &\quad - \int_0^{t_f} \left( \lambda^{\mathrm{T}} \frac{\partial \mathbf{F}}{\partial \gamma_e} \right) \mathrm{d}t\end{aligned} \tag{20}$$

The partial derivatives of the force $\mathbf{F}$ with respect to $\mathbf{x}$ and $\gamma_e$ are as follows:

$$\begin{aligned}\frac{\partial \mathbf{F}}{\partial \mathbf{x}} &= \frac{\partial \mathbf{F}}{\partial \rho} \frac{\partial \rho}{\partial \mathbf{x}} + \frac{\partial \mathbf{F}}{\partial \nabla \rho} \frac{\partial \nabla \rho}{\partial \mathbf{x}} \\ \frac{\partial \mathbf{F}}{\partial \gamma_e} &= \frac{\partial \mathbf{F}}{\partial \rho} \frac{\partial \rho}{\partial \gamma_e} + \frac{\partial \mathbf{F}}{\partial \nabla \rho} \frac{\partial \nabla \rho}{\partial \gamma_e}\end{aligned} \tag{21}$$

Since the derivative of a constant force such as $\mathbf{F}_{\text{gravity}}$ is zero, only the derivative of the contact force $\mathbf{F}_{\text{contact}}$ given in Eq. (6) is required. The partial derivatives of this force with respect to $\rho$ and $\nabla\rho$ are as follows:

$$\begin{aligned}\frac{\partial \mathbf{F}}{\partial \rho} &= k \frac{\nabla \rho}{\|\nabla \rho\|^2} \left( (\rho_{\text{wall}} - \rho) \frac{\mathrm{d}s(\rho)}{\mathrm{d}\rho} - s(\rho) \right) \\ &\approx - \frac{k\, s(\rho) \nabla \rho}{\|\nabla \rho\|^2}\end{aligned} \tag{22}$$

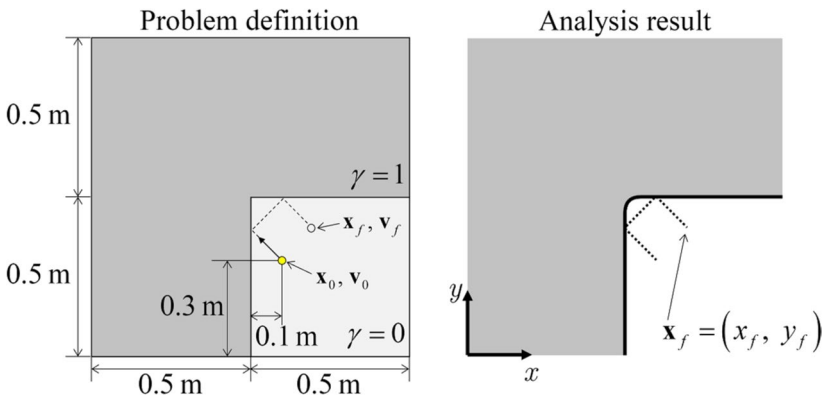


**Fig. 7** Problem definition for comparing the adjoint sensitivity and the sensitivity obtained by the finite difference method and the analysis result (particle: $\mathbf{v}_0 = (-1, \ 1)$ m/s, $t_f = 0.3$ s, $k = 10^6$ N/m and wall: $\rho_{\text{wall}} = 0.5$, $r_{\min}^{(1)} = 2.5$ pixels, $r_{\min}^{(2)} = 11$ pixels)

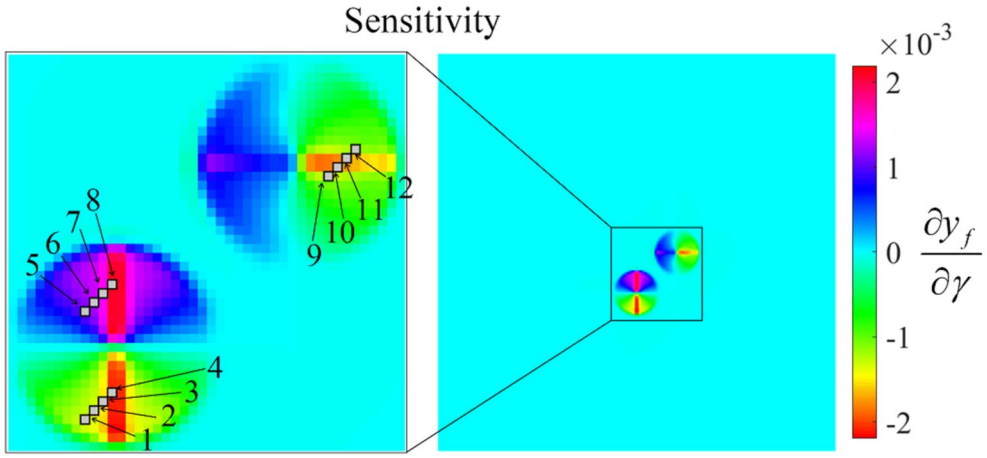


*S*-shape function, $\Delta t = 5\times10^{-6}$ s

| Element # | FDM | Adjoint | Error (%) |
|---|---|---|---|
| 1 | -1.582E-03 | -1.332E-03 | 15.79 |
| 2 | -1.584E-03 | -1.334E-03 | 15.78 |
| 3 | -1.819E-03 | -1.512E-03 | 16.85 |
| 4 | -2.566E-03 | -2.082E-03 | 18.88 |
| 5 | 1.240E-03 | 1.074E-03 | 13.40 |
| 6 | 1.498E-03 | 1.268E-03 | 15.33 |
| 7 | 1.820E-03 | 1.512E-03 | 16.93 |
| 8 | 2.582E-03 | 2.093E-03 | 18.93 |
| 9 | -1.139E-03 | -1.289E-03 | 13.16 |
| 10 | -1.618E-03 | -1.795E-03 | 10.96 |
| 11 | -1.573E-03 | -1.725E-03 | 9.66 |
| 12 | -1.095E-03 | -1.188E-03 | 8.44 |

*S*-shape function, $\Delta t = 10^{-6}$ s

| Element # | FDM | Adjoint | Error (%) |
|---|---|---|---|
| 1 | -1.659E-03 | -1.723E-03 | 3.86 |
| 2 | -1.671E-03 | -1.725E-03 | 3.27 |
| 3 | -1.889E-03 | -1.956E-03 | 3.55 |
| 4 | -2.629E-03 | -2.692E-03 | 2.39 |
| 5 | 1.339E-03 | 1.389E-03 | 3.75 |
| 6 | 1.582E-03 | 1.640E-03 | 3.70 |
| 7 | 1.897E-03 | 1.956E-03 | 3.09 |
| 8 | 2.636E-03 | 2.707E-03 | 2.67 |
| 9 | -1.168E-03 | -1.204E-03 | 3.10 |
| 10 | -1.659E-03 | -1.698E-03 | 2.38 |
| 11 | -1.605E-03 | -1.641E-03 | 2.24 |
| 12 | -1.119E-03 | -1.135E-03 | 1.44 |

*S*-shape function, $\Delta t = 5\times10^{-7}$ s

| Element # | FDM | Adjoint | Error (%) |
|---|---|---|---|
| 1 | -1.687E-03 | -1.690E-03 | 0.16 |
| 2 | -1.689E-03 | -1.692E-03 | 0.18 |
| 3 | -1.903E-03 | -1.918E-03 | 0.78 |
| 4 | -2.596E-03 | -2.640E-03 | 1.67 |
| 5 | 1.318E-03 | 1.363E-03 | 3.40 |
| 6 | 1.596E-03 | 1.608E-03 | 0.75 |
| 7 | 1.895E-03 | 1.918E-03 | 1.18 |
| 8 | 2.641E-03 | 2.654E-03 | 0.51 |
| 9 | -1.160E-03 | -1.181E-03 | 1.85 |
| 10 | -1.641E-03 | -1.669E-03 | 1.73 |
| 11 | -1.614E-03 | -1.616E-03 | 0.14 |
| 12 | -1.104E-03 | -1.120E-03 | 1.49 |

Unit step function, $\Delta t = 5\times10^{-7}$ s

| Element # | FDM | Adjoint | Error (%) |
|---|---|---|---|
| 1 | -1.681E-03 | -1.687E-03 | 0.36 |
| 2 | -1.689E-03 | -1.689E-03 | 0.01 |
| 3 | -1.910E-03 | -1.914E-03 | 0.20 |
| 4 | -2.617E-03 | -2.635E-03 | 0.68 |
| 5 | 1.328E-03 | 1.360E-03 | 2.46 |
| 6 | 1.600E-03 | 1.605E-03 | 0.36 |
| 7 | 1.897E-03 | 1.914E-03 | 0.87 |
| 8 | 2.630E-03 | 2.649E-03 | 0.72 |
| 9 | -1.153E-03 | -1.181E-03 | 2.42 |
| 10 | -1.653E-03 | -1.668E-03 | 0.95 |
| 11 | -1.588E-03 | -1.616E-03 | 1.72 |
| 12 | -1.109E-03 | -1.120E-03 | 0.95 |

**Fig. 8** Comparison of the adjoint sensitivity and the sensitivity obtained by the finite difference method (FDM) of the $y$-position of the particle at $t = t_f$

In the above equation, the term, $\left(\rho_{\text{wall}} - \rho\right)\frac{\mathrm{d}s(\rho)}{\mathrm{d}\rho}$, is neglected as the term $\left(\rho_{\text{wall}} - \rho\right)$ becomes small when $\rho$ is near the outline of $\rho_{\text{wall}}$ and the term $\frac{\mathrm{d}s(\rho)}{\mathrm{d}\rho}$ becomes small when $\rho$ has a distance from $\rho_{\text{wall}}$.

$$\frac{\partial \mathbf{F}}{\partial \nabla\rho} = k\left(\rho_{\text{wall}} - \rho\right)s(\rho)\left(\frac{\mathbf{I}}{\|\nabla\rho\|^2} - 2\frac{\nabla\rho\nabla\rho}{\|\nabla\rho\|^4}\right) \tag{23}$$

where $\nabla\rho\nabla\rho$ denotes the dyadic product of the vector $\nabla\rho$ with itself.

From Eq. (20), the subsequent adjoint equation is derived.

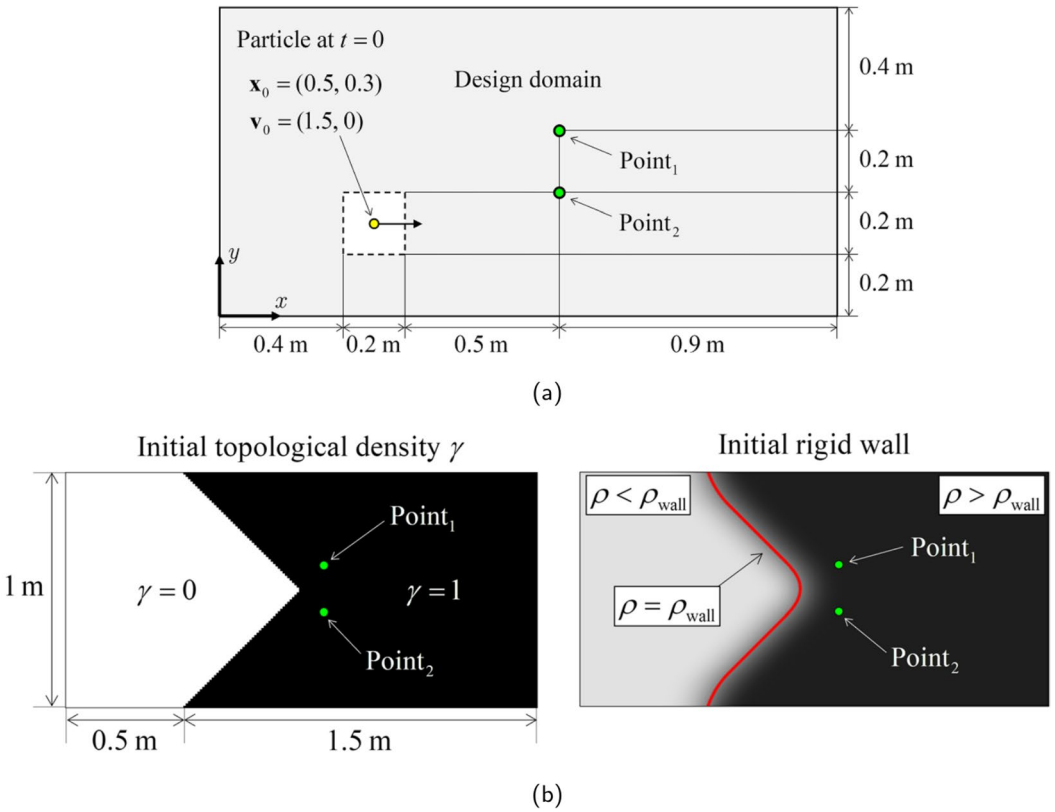


**Fig. 9** Example 1. Problem definition for controlling a particle to pass specified points. **a** The problem definition (particle analysis: $t_f = 0.8$ s, $\Delta t = 2 \times 10^{-5}$ s, $k = 10^6$ N/m and target points: point$_1$ = (1.1, 0.6) and point$_2$ = (1.1, 0.4)) and **b** the initial topological density and the wall ($\rho_{\text{wall}} = 0.5$, $r_{\min}^{(1)} = 2.5$ pixels and $r_{\min}^{(2)} = 15.5$ pixels)

$$\dot{\lambda}^{\mathrm{T}}(t_f) = \frac{1}{m}\left(\frac{\partial c}{\partial \dot{\mathbf{x}}} - \frac{\mathrm{d}}{\mathrm{d}t}\left(\frac{\partial c}{\partial \ddot{\mathbf{x}}}\right)\right)$$
$$\lambda^{\mathrm{T}}(t_f) = -\frac{1}{m}\frac{\partial c}{\partial \ddot{\mathbf{x}}}$$
$$\ddot{\lambda} - \frac{1}{m}\left(\frac{\partial \mathbf{F}}{\partial \mathbf{x}}\right)^{\mathrm{T}}\lambda = \frac{1}{m}\left(-\frac{\partial c}{\partial \mathbf{x}}^{\mathrm{T}} + \frac{\mathrm{d}}{\mathrm{d}t}\left(\frac{\partial c}{\partial \dot{\mathbf{x}}}\right)^{\mathrm{T}} - \frac{d^2}{dt^2}\left(\frac{\partial c}{\partial \ddot{\mathbf{x}}}\right)^{\mathrm{T}}\right) \tag{24}$$

By solving Eq. (24) with the time reversal scheme and using $\lambda$ which satisfies the adjoint equation, the sensitivity can be determined as follows:

$$\frac{\mathrm{d}L}{\mathrm{d}\gamma_e} = -\int_0^{t_f}\left(\lambda^{\mathrm{T}}\frac{\partial \mathbf{F}}{\partial \gamma_e}\right)\mathrm{d}t \tag{25}$$

The Newmark method is employed as the numerical technique for time integration. The accuracy of the analytical sensitivity is validated in the numerical example.

## 2.4 New constraints for trajectory control

In this section, a new constraint is developed to effectively control the trajectory of the particle. This constraint is based on the concept of the minimum distance between a certain point and the trajectory of the particle. The distance between a certain point $\mathbf{x}_0$ and the position of the particle $\mathbf{x}(t)$ at an arbitrary time $t$ is given by:

$$d(t) = \left\|\mathbf{x}(t) - \mathbf{x}_0\right\|, \quad 0 \le t \le t_f \tag{26}$$

The minimum of this distance, represented as $d_{\min}$ in Fig. 6a, can be approximated using the $p$-norm as follows:

$$d_{\min} \approx \left(\int_0^{t_f} d(t)^{-p}\,\mathrm{d}t\right)^{-1/p} \tag{27}$$

If this value is sufficiently small, as illustrated in Fig. 6b, it implies that the particle passes through the point $\mathbf{x}_0$. Conversely, a large value indicates that the particle does not traverse through that point. Using these properties, constraints can be imposed to make the particle pass through or avoid a specific point. Mathematically, the following function serves as the constraint:

$$g(\mathbf{x}, \mathbf{x}_o) = \left(\int_0^{t_f} \left\|\mathbf{x} - \mathbf{x}_o\right\|^{-p}\,\mathrm{d}t\right)^{-1/p} \tag{28}$$

where $g(\mathbf{x}, \mathbf{x}_0)$ denotes the approximated minimum distance between the point $\mathbf{x}_0$ and the particle's trajectory.

To determine the sensitivity of this function, the formula introduced in Sect. 2.3 is employed. To apply the equation

from Sect. 2.3, the function $g$ is modified to $f(\mathbf{x}, \mathbf{x}_0)$ and by substituting $c$ with the appropriate function, the derivative of $f$ can be obtained as follows:

$$\begin{aligned} f(\mathbf{x}, \mathbf{x}_o) &= \int_0^{t_f} \left\| \mathbf{x} - \mathbf{x}_o \right\|^{-p} \mathrm{d}t \\ c_g(\mathbf{x}) &= \left\| \mathbf{x} - \mathbf{x}_o \right\|^{-p} \\ \frac{\partial c_g}{\partial \mathbf{x}} &= -p \cdot c_g^{\,1+\frac{2}{p}} \left( \mathbf{x} - \mathbf{x}_o \right) \end{aligned} \tag{29}$$

The derivative of $f$ is obtained by solving the adjoint equation with the time reversal scheme. Using the chain rule, the derivative of $g$ with respect to $\gamma$ is then determined as follows:

$$\frac{\mathrm{d}g}{\mathrm{d}\gamma_e} = -\frac{1}{p} \left( f^{-\frac{1}{p}-1} \right) \frac{\mathrm{d}f}{\mathrm{d}\gamma_e} \tag{30}$$

Several examples using such constraints for the particle to pass through or to bypass a particular point are provided in Sect. 3.

## 3 Numerical examples

In this section, numerical examples of the topology optimization considering particle collisions using the method introduced in this paper are provided. The Newmark scheme ($\beta = 1/6,\ \gamma = 1/3$) is utilized for the simulation of the transient particle motion. Firstly, to validate the accuracy of the sensitivity analysis presented in this study, it is compared with the numerically computed sensitivity. Subsequently, three optimization problems are addressed using the MMA (Method of Moving Asymptotes) as the optimization algorithm (Svanberg 1987).

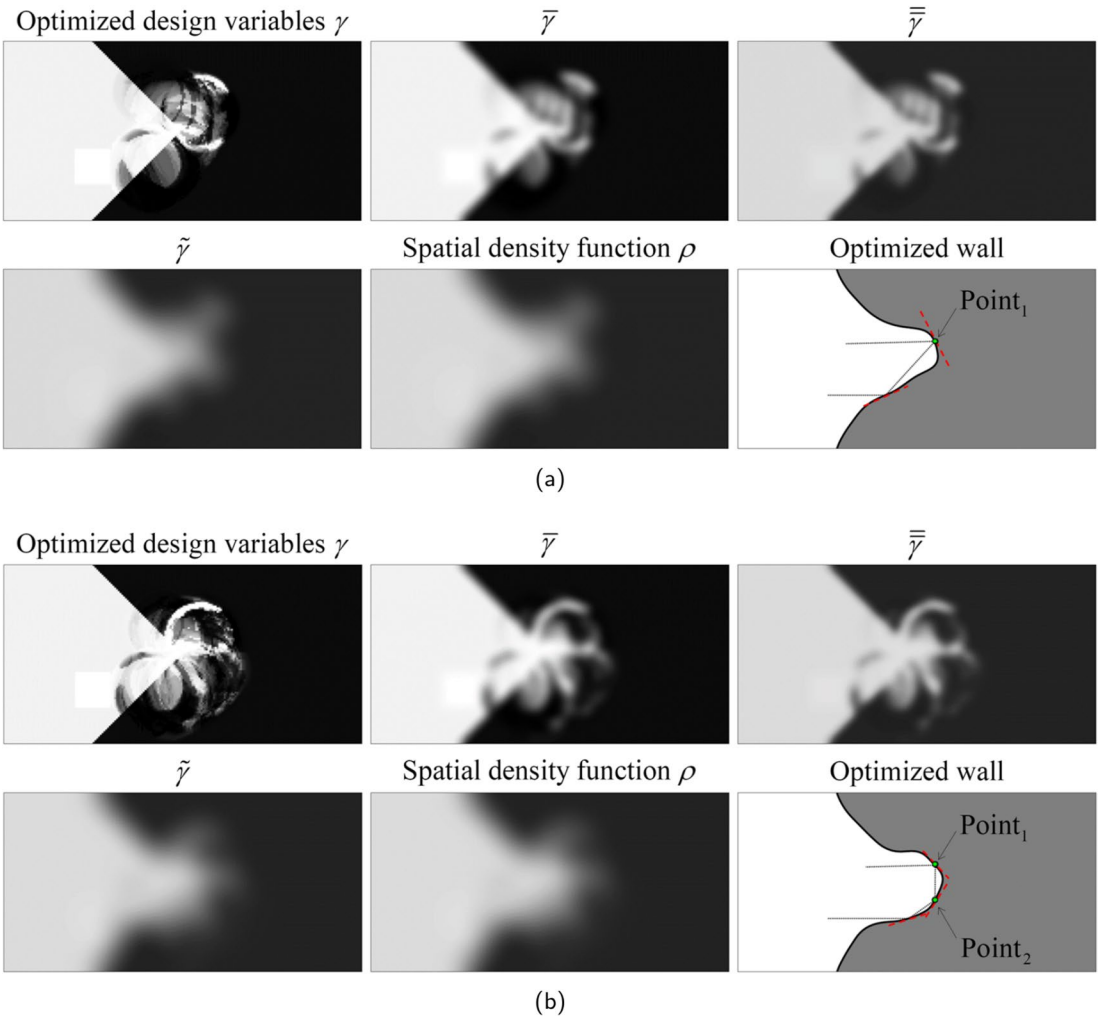


**Fig. 10** Optimization results of Example 1. **a** An optimization result with the constraint of passing through point 1 rendered by green color only and **b** an optimization result with the constraint of passing through both points 1 and 2

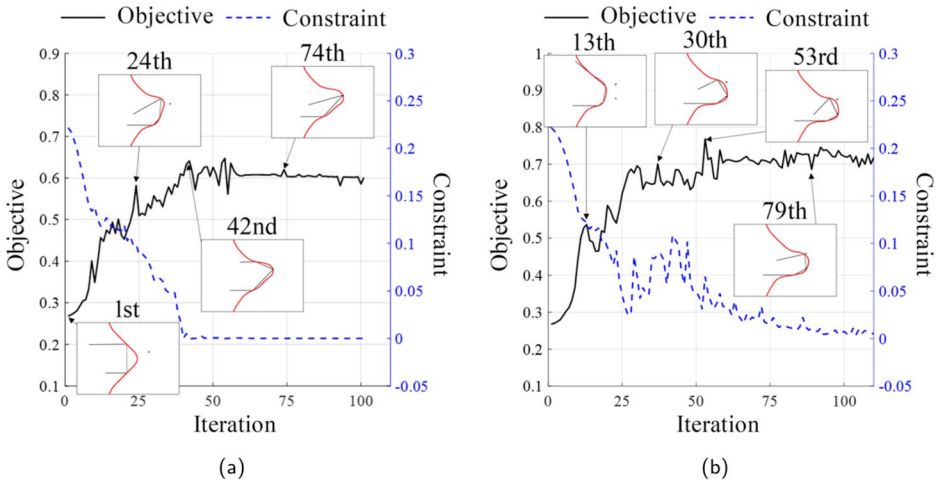


**Fig. 11** The optimization histories of Example 1. The optimization histories of the problems with the constraint of passing through **a** point 1 only and **b** both points 1 and 2

### 3.1 Sensitivity analysis

Before proceeding with numerical examples considering particle-rigid wall contact, the present sensitivity analysis is validated by comparing it with the numerical sensitivity obtained by the finite difference method (FDM). Figures 7 and 8 consider the sensitivity of the final position of the particle when the particle contacts twice. The position of the particle at the final time is obtained as follows:

$$(x_f,\ y_f) = \int_0^{t_f} \dot{\mathbf{x}}\, \mathrm{d}t \tag{31}$$

The final position in $y$-direction, $y_f$, is used for the objective function to compare the sensitivities in this example. The entire mesh is constructed as 100 by 100 and the time steps are set as intervals of $5 \times 10^{-6}$ s, $1 \times 10^{-6}$ s and $5 \times 10^{-7}$ s, respectively. The initial velocity of the particle is $(-1, 1)$ m/s and the final time $t_f$ is set to 0.3 s. With the lowest time step (i.e., $5 \times 10^{-7}$ s), the two functions for interpolating the force exerted on the particle by the rigid wall (the $S$-shape function, $s_{S\text{-shape}}$, and the unit step function, $s_{\text{unit}}$, in Eq. (7)) are compared. Consistent with previous particle topology optimization studies, the sensitivity results with smaller time step are more accurate. However, when the time step becomes excessively small, there are problems of the accumulation of numerical errors and long computational time. As summarized in Fig. 8, even if the time step $\Delta t$ is not sufficiently small, the trend of the adjoint sensitivity is generally consistent to the sensitivity results by FDM. To obtain the accurate sensitivity and save the computational costs,

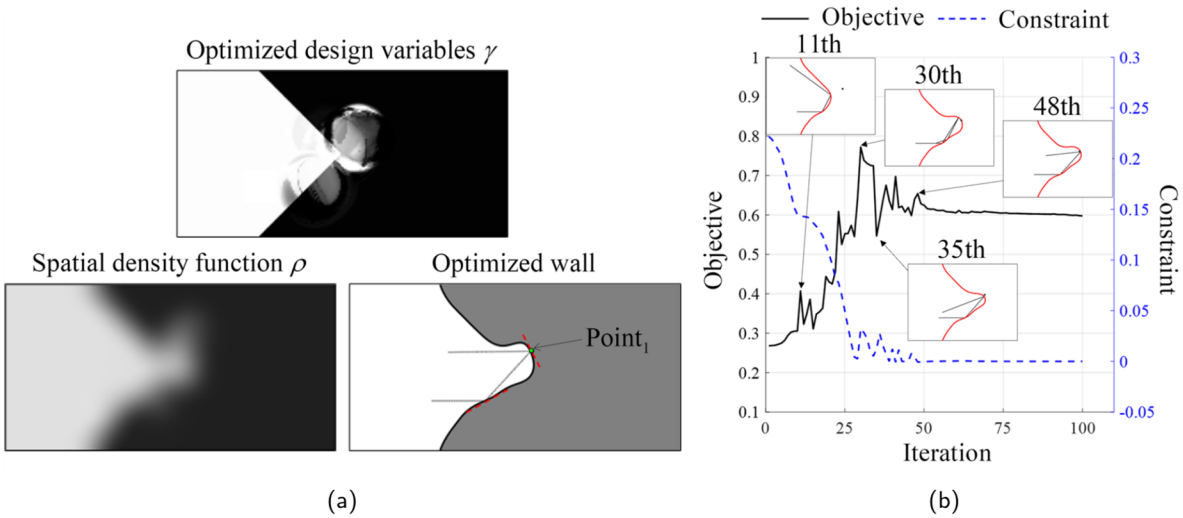


**Fig. 12** An optimization result of Example 1 with the contact force interpolated by $s_{S\text{-shape}}$ function. **a** An optimized layout and **b** optimization history

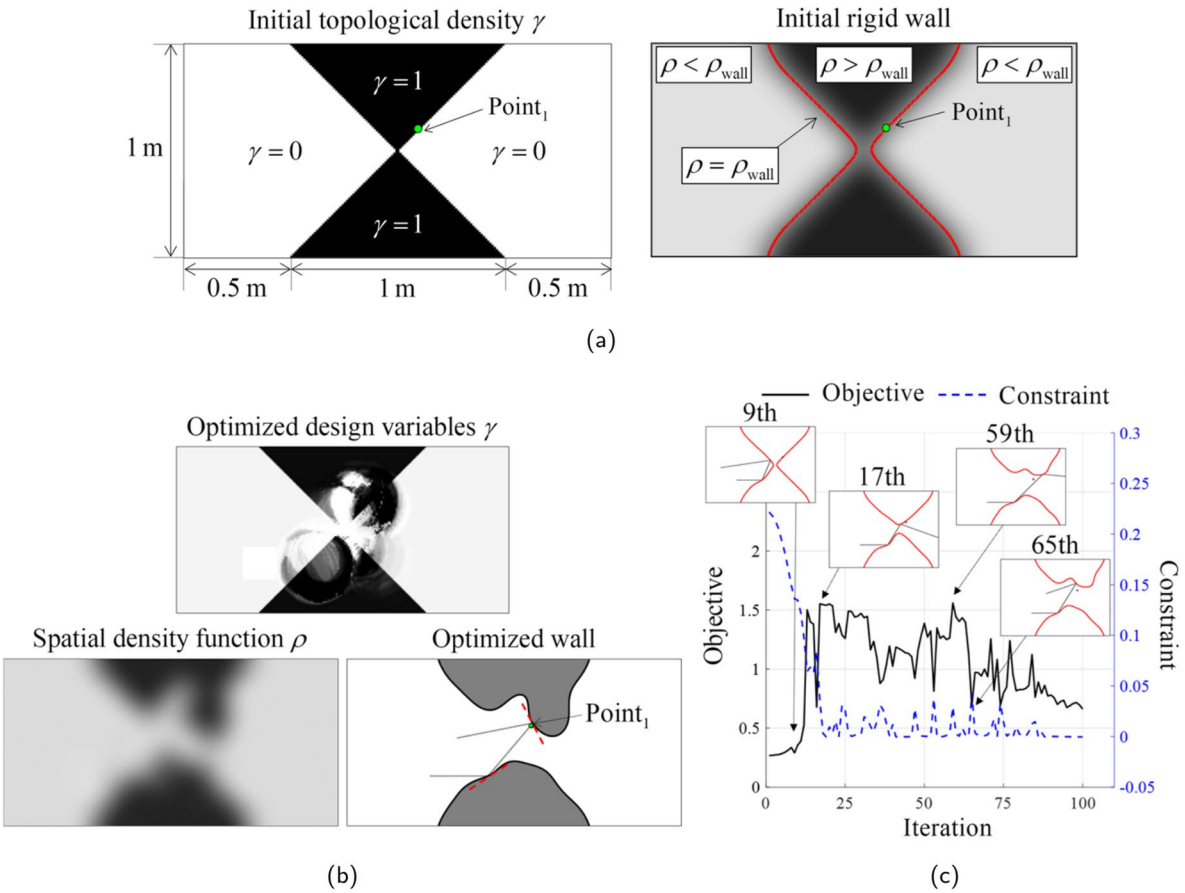


**Fig. 13** Initial design and optimization result for Example 1 with a different initial design. **a** An initial design, **b** optimized result and **c** optimization history

the selection of an appropriate time step size is necessary. When calculating the force, there is no significant difference between using the *S*-shape function ($s_{S\text{-shape}}$) and the unit step function ($s_{\text{unit}}$) for computing the force. However, using the *S*-shape function with high parameter can cause the numerical problems. Therefore, the unit step function is utilized in the interpolation of the contact force in the rest of the examples, unless otherwise noted.

## 3.2 Example 1: Controlling particle to pass specified points

For the first example, topology optimization involving the particle collision is performed using the present sensitivity analysis. The analysis domain is set as Fig. 9a. The objective function is to set as the $x$ or $y$ position of particle and the constraint presented in Sect. 2.4 is employed to ensure that particle of interest passes through designated points or locations. This example solves two optimization problems. The first optimization problem is to find out an optimized wall making particle pass through the point 1 only while minimizing the x location at the final time. The second problem is similar to the first example except that the optimization formulation imposes the condition that a particle should pass the two points or locations marked by the green circles in Fig. 9b. The point and the locations of the point are designated to find out an optimized and smoothed reflecting wall. The particle starts at the position (0.5, 0.3) and the area near the initial particle position is excluded from the design domain to avoid for the particle to locate in the inner region of the solid initially. The initial design variables are set to 0 and 1 in Fig. 9(b: left). These initial variables result in the smooth rigid wall shown in Fig. 9(b: right). Creating a reasonable initial structure is crucial to perform the optimization because the sensitivity values of the parts away from where the particle contact occurs approach zero.

The optimization formulation of this example is set as follows:

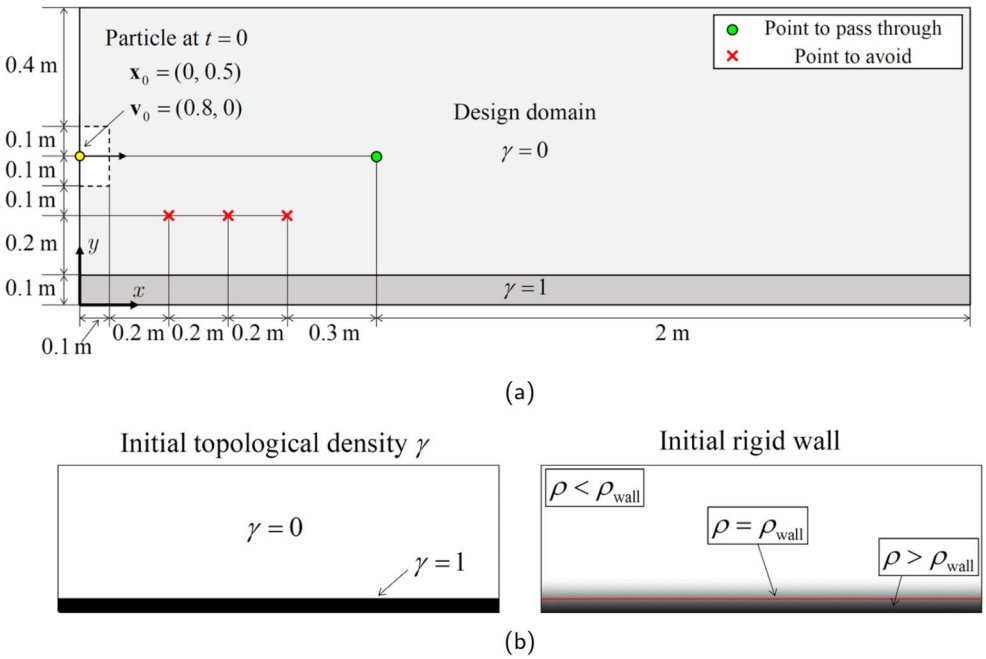


**Fig. 14** Example 2. A trajectory optimization to avoid target points. **a** The problem definition (particle analysis: $t_f = 0.8$ s, $\Delta t = 5 \times 10^{-6}$ s, $k = 10^6$ N/m, $g = (0, -9.81)\,\text{m/s}^2$, the points to avoid: (0.3, 0.3), (0.5, 0.3), (0.7, 0.3), the point to pass through: (1, 0.5), rigid wall: $\rho_{\text{wall}} = 0.5$, $r_{\text{min}}^{(1)} = 2.5$ pixels and $r_{\text{min}}^{(2)} = 15.5$ pixels) and **b** the initial topological density and the initial rigid wall

$$\begin{aligned} &\underset{\gamma}{\text{Minimize}}\ x_f, \\ &\text{subject to}\ \ m\ddot{\mathbf{x}} = \mathbf{F}_{\text{contact}}(\mathbf{x}, \gamma), \\ &\qquad\qquad g(\mathbf{x}, \mathbf{x}_{\text{target}}^{(i)}) \le \varepsilon, \\ &\qquad\qquad 0 \le \gamma_e \le 1 \quad (e = 1,\ 2,\ \cdots,\ \text{NE}), \end{aligned} \tag{32}$$

where $\mathbf{x}_{\text{target}}^{(1)}$ and $\mathbf{x}_{\text{target}}^{(2)}$ denote the points 1 at (1.1, 0.4) and 2 at (1.1, 0.6), respectively. The objective function $x_f$ is the $x$-direction position of the particle at time $t_f$ and the $\varepsilon$ is set as 0.01. The time $t_f$ is 0.8 s and is discretized into 40,000 steps. The design domain in Fig. 9a is discretized into 200 by 100 elements. This example solves the problem for the two cases: one with one constraint ($i = 1$) and another with the two constraints ($i = 1,\ 2$). The range for the design variable $\gamma_e$ is from 0 to 1. In each iteration in the optimization process, the changes in the design variables is restricted lower than 0.05. The force exerted on the particle by the wall is interpolated using Eq. (6), where the unit step function is utilized for the function $s(\rho)$. The initial position $\mathbf{x}_0$ and velocity $\mathbf{v}_0$ of the particle are set as (0.5, 0.3) m and (1.5, 0) m/s, respectively. The gravity force is not considered in this example.

By solving these optimization problems, the designs in Fig. 10 for the particle to pass through the desired points are obtained while $x_f$ is minimizing as Fig. 10. In Fig. 10a, the design is obtained to pass through one point, while in Fig. 10b, the particle passes through two points. The objective values of each of the designs are 0.6009 and 0.7097, respectively. The higher optimization value is caused by the smaller feasible region when two constraints are imposed. In the optimized results, changes in design occur exclusively in the areas adjacent to the contact points because the sensitivities have non-zero values only near the contact points. Furthermore, the results indicate that the target points become the contact points. This makes sense because, to minimize $x_f$, the particle should turn to the left as quickly as possible after passing through the contact points. The optimization history is illustrated in Fig. 11, where both the objective and constraint functions are depicted. For the constraints, the plot shows the left-hand side (LHS) value minus the right-hand side (RHS) value of the constraint. When multiple constraints are employed, the maximum value of LHS minus RHS (which should be less than zero) is plotted. In all remaining examples, constraints are plotted in this manner.

Furthermore, the optimization problem in Fig. 10a is additionally solved by using two different methods. In the first method, the contact force is interpolated using the *S*-shape function. The optimization result, shown in Fig. 12, is nearly identical to the previous result obtained using the unit step function, as shown in Fig. 10a. In the second method, optimization is performed with a different initial design, as shown in Fig. 13a. Since present methodology can be influenced by the initial design, it is important to evaluate the performance with various initial design. The optimization results and history are provided in Fig. 13b, c, respectively. Although the overall geometry

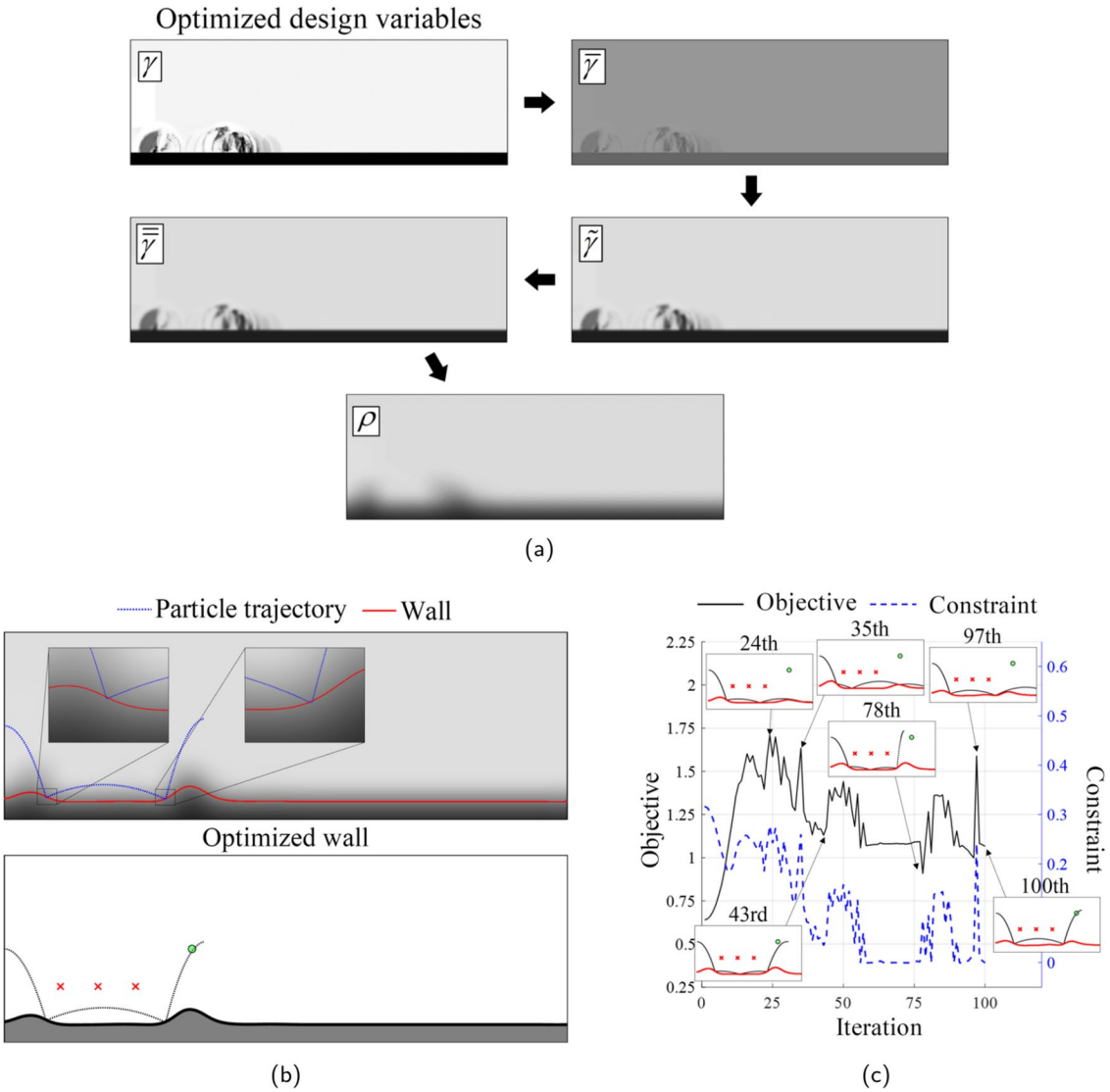


**Fig. 15** Example 2. **a** An optimized result, **b** the particle trajectory and optimized wall and **c** the optimization history

differs from Fig. 10a, the collision location and the angle of the collision surface are similar. These examples confirm that the present methodology can control the trajectory of the particle to pass the specific points.

### 3.3 Example 2: Trajectory optimization to avoid target points under gravity

This example focuses on designing rigid wall that ensures a particle avoids specific points while considering both collisions and gravitational effects. By setting constraints to be larger than a specific value based on Eq. (28) from Sect. 2.4, particle trajectory can be optimized to avoid designated points. Additionally, the constraint that enables the particle to pass through a desired point is also employed. The desired points to pass through and to avoid are represented by a green circle and red crosses, respectively, in Fig. 14a. The point to pass through is located at (1, 0.5) and the points to avoid are set at (0.3, 0.3), (0.5, 0.3) and (0.7, 0.3). These points were chosen to demonstrate the feasibility of constraints designed to prevent particles from passing through regions that were accessible in the unoptimized rigid wall. The design domain is illustrated in Fig. 14a and discretized into 300 by 100 elements. As shown in Fig. 14(b: left), the initial design variables of the upper and lower domain are set to 0 and 1, respectively. This results in initial rigid wall at a distance of 0.1 m from the bottom of the domain as illustrated in Fig. 14(b: right).

To obtain a trajectory of the particle that satisfies these conditions, the following optimization problem is formulated.

$$\begin{aligned} &\underset{\gamma}{\text{Maximize}}\ x_f, \\ &\text{subject to}\ \ g(\mathbf{x}, \mathbf{x}_{\text{pass}}) \le \varepsilon, \\ &\qquad g(\mathbf{x}, \mathbf{x}^{(i)}_{\text{avoid}}) \ge R \quad (i = 1,\ 2,\ 3), \\ &\qquad m\ddot{\mathbf{x}} = \mathbf{F}_{\text{contact}}(\mathbf{x}, \gamma) + \mathbf{F}_{\text{gravity}}, \\ &\qquad 0 \le \gamma_e \le 1 \quad (e = 1,\ 2,\ \cdots,\ \text{NE}), \end{aligned} \tag{33}$$

where the desired point to pass is denoted by $\mathbf{x}_{\text{pass}}$, while the points to avoid are labeled as $\mathbf{x}^{(i)}_{\text{avoid}}$ $(i = 1,\ 2,\ 3)$. The gravity force is denoted by $\mathbf{F}_{\text{gravity}}$. In the constraints, the value of $\varepsilon$ is set to 0.01 m to ensure passing through $\mathbf{x}_{\text{pass}}$, and $R$ is set to 0.1 m due to the placement of avoidance points at 0.2 m intervals. The range of the design variables and the limit for changing the design variables are same as in Example 1. The objective is the maximization of the final position of the particle. The analysis time, $t_f$, for the particle is set to 0.8 s and the time step is set to $5 \times 10^{-6}$ s, resulting in 160,000 discretized time steps. The initial position of the particle, $\mathbf{x}_0$, and the velocity, $\mathbf{v}_0$, are defined to (0, 0.5) m and (0.8, 0) m/s, respectively.

An optimized design ensuring the particle passes through the desired point and avoids the other points is obtained as shown in Fig. 15. The optimized layout contacts with the particle at the two regions. In the optimized rigid wall, the regions apart from the collision regions can be arbitrary shapes as long as it doesn't affect the particle path. This means there are multiple possible solutions except for the collision regions. The design of these other regions depends on the initial design. For instance, the result in Fig. 15 represents one of the optimal designs which is close to the initial layout in Fig. 14b. The optimization history can be found in Fig. 15c. In the optimization history, there are several peaks where the objective appears to be maximized, but the constraints are not satisfied. Since the main focus of this problem is to find a solution that satisfies the constraints, the optimization process is stopped after a certain number of iterations (100) if the constraints are all satisfied. This example verifies that particles can be controlled to avoid certain areas by utilizing the present constraints.

### 3.4 Example 3: Manipulating multiple particles

In this example, the purpose is to optimize the trajectories of multiple particles so that they converge to a single point when they collide with the wall. The two cases are considered: one where gravity is taken into account and another where it is neglected. The influence of the number of particles is also observed by solving the optimization problem for the cases with 9, 19 and 29 particles. Moreover, the optimization will be carried out for two distinct times ($t_f = 1.2$ s and 0.6 s) to understand the effect of the analysis time.

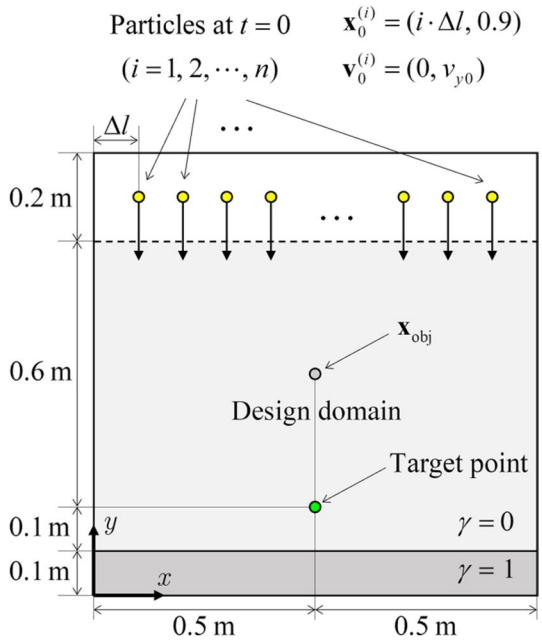


**Fig. 16** Example 3. Problem definition for manipulating multiple particles (particle analysis: $\Delta t = 5 \times 10^{-5}$ s, $k = 10^6$ N/m and rigid wall: $\rho_{\text{wall}} = 0.5$, $r^{(1)}_{\text{min}} = 2.5$ pixels and $r^{(2)}_{\text{min}} = 15.5$ pixels)

The analysis of the particles being dropped from a height of 0.9 m in the square domain as shown in Fig. 16 is conducted. The particles are uniformly distributed with a distance of $\Delta l$. The design domain is defined as follows:

$$\{(x,\ y)\,|0 \le x \le 1,\ 0.1 \le y \le 0.8\}, \tag{34}$$

where the entire square domain is discretized into 101 by 100 elements. The number of elements in $x$-direction is set to the odd number, 101, to avoid asymmetry problems that can be caused by numerical errors in computing for the particle falling from the center. The initial design variables are set to 0 for the upper region ($y \ge 0.1$) and 1 for the lower region ($y < 0.1$), generating the initial wall 0.1 m above from the bottom. The objective function aims to minimize the distance between the final position of the central particle in Fig. 16 and its analytically calculated position in the initial design. This ensures that the optimized layout passes through the bottom center point (0.5, 0.1). Similar to Example 2, the optimization process terminates when all constraints are satisfied and the specific number of iterations, i.e., 100 iterations, have been proceeded. The optimization formulation is given as follows:

$$\begin{aligned} &\underset{\gamma}{\text{Minimize}}\ \left\| \mathbf{x}_f^{(c)} - \mathbf{x}_{\text{obj}} \right\|^2, \\ &\text{subject to}\ \ m\ddot{\mathbf{x}} = \mathbf{F}_{\text{contact}}(\mathbf{x}, \gamma) + \mathbf{F}_{\text{gravity}}, \\ &\qquad g(\mathbf{x}^{(i)}, \mathbf{x}_{\text{target}}) \le \varepsilon \quad (i = 1,\ 2,\ \cdots,\ \text{NP}), \\ &\qquad 0 \le \gamma_e \le 1 \quad (e = 1,\ 2,\ \cdots,\ \text{NE}), \end{aligned} \tag{35}$$

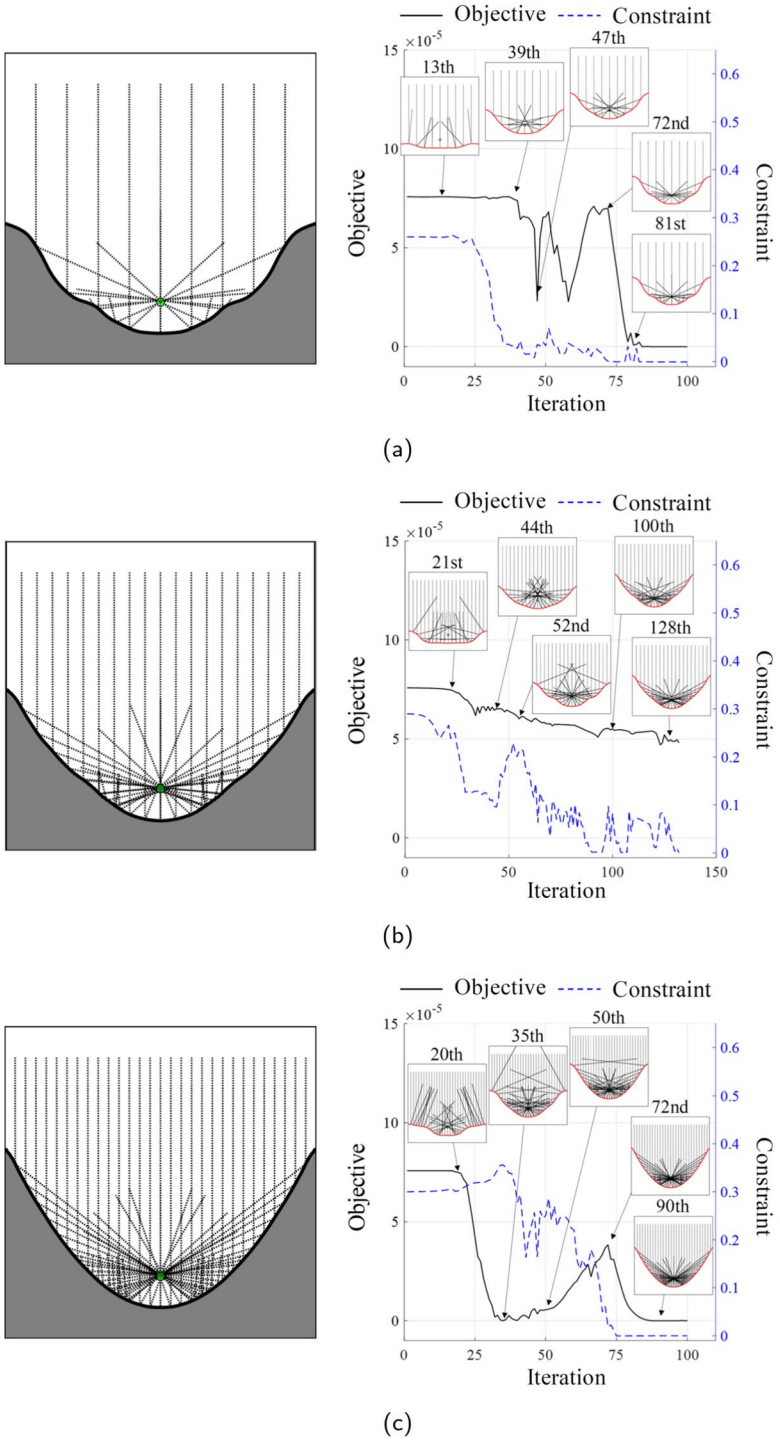


**Fig. 17** Example 3. Optimized results without considering the gravity force and their optimization histories (the initial y-direction velocity = −1 m/s, $t_f$ = 1.2 s and the number of **a** 9 particles, **b** 19 particles and **c** 29 particles)

where the number of particles being dropped is denoted by NP, the position of the central particle at time $t = t_f$ is denoted by $\mathbf{x}_f^{(c)}$ and $\mathbf{x}_{\text{obj}}$ is the analytically calculated position of the $c$-th particle at time $t = t_f$. The desired point to pass, $\mathbf{x}_{\text{target}}$, is set to (0.5, 0.2) and the position of the $i$-th particle, $\mathbf{x}_0^i$, is equal to $(i\Delta l, 0.9)$, where $\Delta l$ is $1/(\text{NP}+1)$ m. The gravitational force, $\mathbf{F}_{\text{gravity}}$, is set to $m\mathbf{g}$ when gravity is considered and is set to $\mathbf{0}$ otherwise. The design constraints and the other parameters are consistent with the previous examples.

The first problem is optimization without considering gravity and sets the initial velocity to $(0, v_{y0})$, where $v_{y0}$ is −1 m/s and $t_f$ is 1.2 s. In this case, $\mathbf{x}_{\text{obj}}$ is computed as (0.5, 0.5). By setting NP to 9, 19 and 29, the results in Fig. 17 are obtained, respectively. Note that the latter case obtains

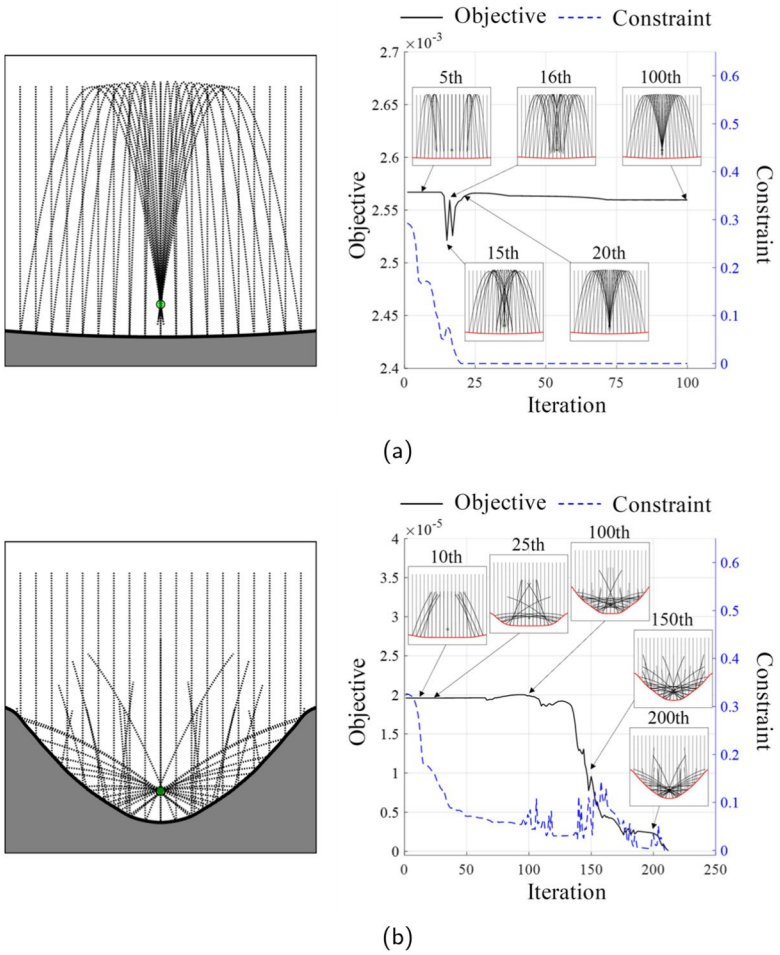


**Fig. 18** Example 3. Optimized results with the gravity force and their optimization histories (the number of particles: 19, the initial $y$-direction velocity: 0 m/s, the gravity acceleration: $(0, -9.81)$ m/s$^2$, **a** $t_f = 1.2$ s and **b** $t_f = 0.6$ s)

the smoother rigid wall because the increase in the number of particles results in approaching the parabolic shaped rigid wall which is the theoretical optimized solution for converging to a point when particles are incident in parallel (See Appendix 2 for the theoretical solution). The second problem incorporates gravity and sets the initial velocity to $\mathbf{0}$. For $t_f$ values of 1.2 s and 0.6 s, $\mathbf{x}_{\text{obj}}$ is computed as (0.5, 0.1452) and (0.5, 0.6884), respectively, and both cases utilize 19 particles. As shown in Fig. 18, the parabolic trajectories pass through the desired point at each of the times. Fig. 19 presents comparisons between the optimized results and the theoretical solutions for the particles to pass through the target point. Figure 19a demonstrates that with the larger number of particles, the shape of optimized wall approaches the theoretical solution. When gravity is applied to the particles, there are two theoretical solutions as shown in Fig. 19b and the optimized results are close to these solutions. These theoretical solutions are derived in Appendix 2. These results validate that the current method can control the particles effectively even with multiple particles.

## 4 Conclusions

In this study, we have developed a new topology optimization methodology that controls the trajectory of particles while considering their contact with rigid wall layouts. The conventional topology optimization faces the two primary challenges in accounting for particle-rigid wall contact: the discontinuous behavior of the particle contact and the non-smooth geometry of the topological design. These challenges were successfully addressed by using the present spring contact model and transforming the design variables. By applying density filtering and the $S$-shape function, the design variables were mapped into a smoothly shaped structural design. Subsequently, the present contact model calculates the force exerted on particles during

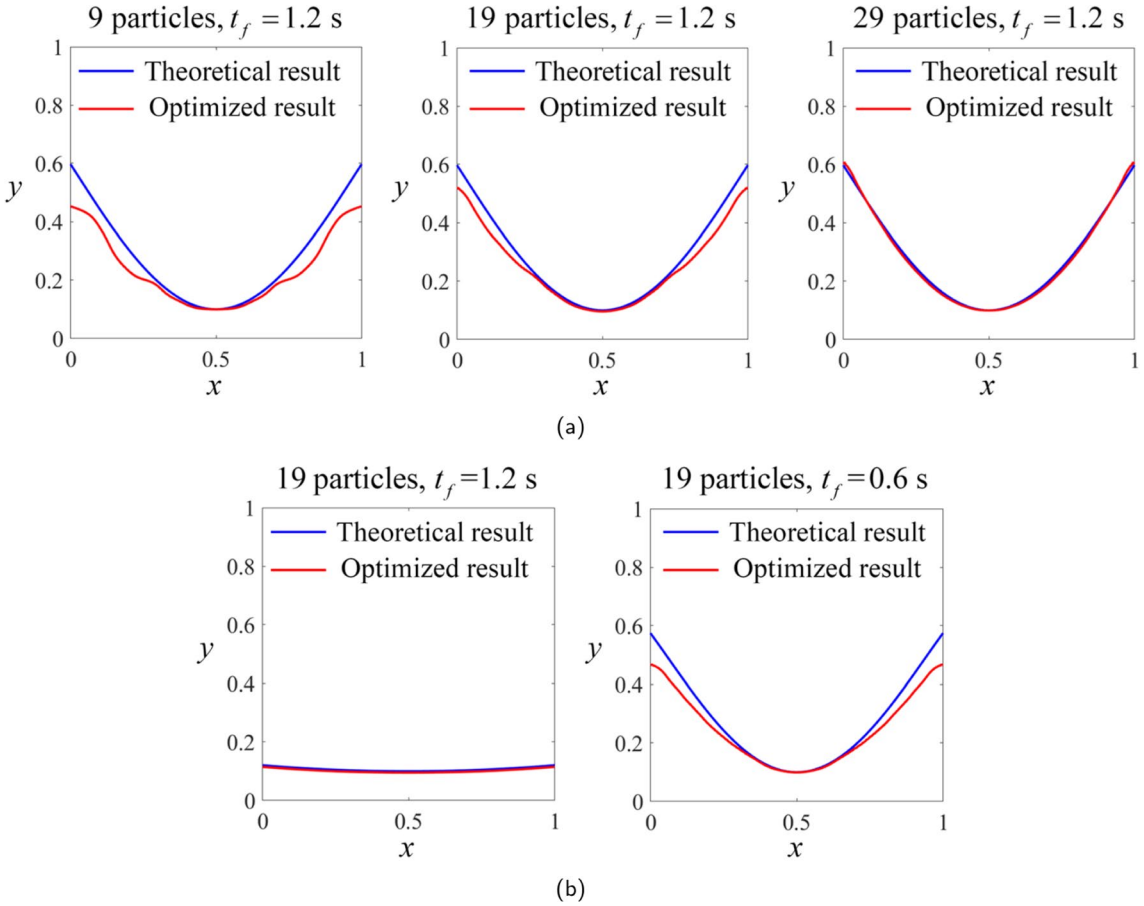


**Fig. 19** Comparison between the analytic solutions and the optimized results in **a** Fig. 17 and **b** Fig. 18

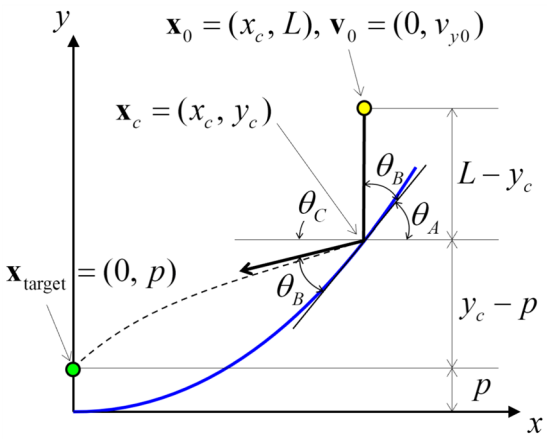


**Fig. 20** Schematic drawing for obtaining the analytic interface curve for particles to pass the target point

contact with the rigid wall. Following the force calculation, the sensitivity of the force was computed analytically and several numerical examples of the topology optimization of the particle path were conducted. The trajectories of the particles were controlled using the constraint for the particles to pass through or to avoid a designated point. In future work, by integrating this model with solid or fluid domains, these domains could be optimized simultaneously while considering the particle contact phenomena. In summary, this study has introduced a novel methodology for topology optimization that incorporates particle-rigid wall contact, utilizing an innovative contact model and a constraint to control the particle trajectories.

## Appendix 1: Mapping from element-wise to nodal design variables using PDE filter

In this study, element-wise design variables are mapped to nodal design variables through Eq. (13). In Sect. 2.2, the equation for mapping from $\tilde{\boldsymbol{\gamma}}$ to $\boldsymbol{\rho}$ in Eq. (16) is derived from Eq. (13). This section aims to show that a similar expression can also be derived from the PDE filter introduced in Andreassen et al. (2011) and discusses the differences between the two approaches. The partial differential equation employed in the PDE filter is given as follows.

$$\begin{aligned} -R_{\min}^2 \nabla^2 \rho + \rho &= \tilde{\gamma} \quad \text{on } \Omega \\ \nabla \rho \cdot \mathbf{n} &= 0 \quad \text{on } \partial\Omega \end{aligned} \tag{36}$$

where $R_{\min}$ represents the radius of filtering. The above PDE can be rewritten in weak form as follows.

$$\begin{aligned} \int_\Omega \phi\tilde{\gamma} \, \mathrm{d}\Omega &= \int_\Omega \phi\left(-R_{\min}^2 \nabla^2 \rho + \rho\right) \mathrm{d}\Omega \\ &= \int_\Omega \left(R_{\min}^2 \nabla\phi \nabla\rho + \phi\rho\right) \mathrm{d}\Omega \end{aligned} \tag{37}$$

The discretization using the finite element method yields the following matrix form.

$$\begin{aligned} \mathbf{Q}\tilde{\boldsymbol{\gamma}} &= (R_{\min}^2 \mathbf{K} + \mathbf{M})\boldsymbol{\rho} \\ \boldsymbol{\rho} &= \left(R_{\min}^2 \mathbf{K} + \mathbf{M}\right)^{-1} \mathbf{Q}\tilde{\boldsymbol{\gamma}} \end{aligned} \tag{38}$$

where $\mathbf{M}$ and $\mathbf{Q}$ are defined in Sect. 2.2 and $\mathbf{K}$ is defined as follows:

$$\mathbf{K} = \sum_{e=1}^{NE} \int_{\Omega_e} \frac{\partial \mathbf{N}_e^{\mathrm{T}}}{\partial \mathbf{x}} \left( \frac{\partial \mathbf{N}_e^{\mathrm{T}}}{\partial \mathbf{x}} \right)^{\mathrm{T}} \mathrm{d}\Omega \tag{39}$$

It is noteworthy that, when $R_{\min}$ is set to zero, the resulting equation corresponds to Eq. (16) which computes the nodal density $\boldsymbol{\rho}$ used in the present study.

## Appendix 2: Theoretical solution for particles to pass a specified point

This section explains the theoretical derivation of a curve which enables that the particles falling parallel to the $y$-axis pass through a specific point, $\mathbf{x}_{\text{target}} = (0, p)$, after one perfectly elastic collision with the curve. The contact point is denoted by $\mathbf{x}_c = (x_c, y_c)$ and the initial position and velocity are denoted by $\mathbf{x}_0 = (x_c, L)$ and $\mathbf{v}_0 = (0, v_{y0})$, respectively. As shown in Fig. 20, the angle between the tangent line at the contact point and the $x$-axis is defined as $\theta_A$ and its slope is described as follows:

$$\left.\frac{\mathrm{d}y}{\mathrm{d}x}\right|_{\mathbf{x}=\mathbf{x}_c} = \tan\theta_A \tag{40}$$

The angles between the tangent line and the two lines, the incident and reflected lines, are identical and denoted by $\theta_B$. $\theta_C$ represents the angle between the reflected line and the $x$-axis. These angles satisfy the following relationships.

$$\begin{aligned} \theta_A + \theta_B &= \frac{\pi}{2}, \\ \theta_C &= \theta_A - \theta_B \end{aligned} \tag{41}$$

Utilizing the tangent addition formula with the relationship in Eq. (41), $\tan(\theta_C)$ is derived and subsequently $\tan(\theta_A)$ is obtained as follows:

$$\begin{aligned} \tan\theta_C &= \frac{\tan\theta_A - 1/\tan\theta_A}{2}, \\ \tan\theta_A &= \tan\theta_C + \sqrt{1 + \tan^2\theta_C} \end{aligned} \tag{42}$$

The $\tan\theta_C$ is obtained by the procedure from Eq. (43) to Eq. (45). With the initial velocity of $\mathbf{v}_0$, the velocity of a particle at the contact point is determined as follows:

$$\|\mathbf{v}_c\| = \sqrt{\|\mathbf{v}_0\|^2 + 2g(L - y_c)} \tag{43}$$

After the contact, the velocity of the particle in the $x$-direction becomes $\|\mathbf{v}_c\| \cos\theta_C$ and a time to reach from the contact to the target point is given by $t = x_c \Big/ \left(\|\mathbf{v}_c\| \cos\theta_C\right)$. To reach the target point, the vertical displacement of the particle for this time should be the $y$-directional distance between the contact and target points (i.e., $y_c - p$) and the following equations are obtained.

$$\begin{aligned} y_c - p &= \|\mathbf{v}_c\| \sin\theta_C t + \frac{1}{2} g t^2 \\ &= x_c \tan\theta_C + \frac{g x_c^2}{4g(L - y_c) + 2v_{y0}^2} \left(\tan^2\theta_C + 1\right) \end{aligned} \tag{44}$$

$$\tan\theta_C = \begin{cases} \dfrac{-1 \pm \sqrt{1 - \dfrac{\left(\frac{x_c^2}{2(L-y_c)+v_{y0}^2/g} - y_c + p\right)}{2(L-y_c)+v_{y0}^2/g}}}{x_c \Big/ \left(2(L-y_c)+v_{y0}^2/g\right)}, & g \neq 0, \\ \dfrac{y_c - p}{x_c}, & g = 0 \end{cases} \tag{45}$$

By using Eqs. (40) and (42), the following differential equation is derived.

$$\frac{\mathrm{d}y}{\mathrm{d}x} = \tan\theta_C + \sqrt{1 + \tan^2\theta_C}, \quad y(0) = 0 \tag{46}$$

where $\tan\theta_C$ is substituted by Eq. (45) depending on the gravitational acceleration, $g$. Equation (46) yields a single solution in the absence of gravitational forces and has two distinct solutions when the gravity force is applied. The solutions for the two cases (case 1: $g = 0\ \mathrm{m/s^2}$, $v_{y0} = 1\ \mathrm{m/s}$, $L = 0.8\ \mathrm{m}$ and $p = 0.1\ \mathrm{m}$ and case 2: $g = 9.81\ \mathrm{m/s^2}$, $v_{y0} = 0\ \mathrm{m/s}$, $L = 0.8\ \mathrm{m}$ and $p = 0.1\ \mathrm{m}$) are illustrated in Fig. 19a, b, respectively.

**Acknowledgments** This work was supported by the National Research Foundation of Korea (NRF) grant funded by the Korea Government (MSIT) (RS-2024-00351611).

## Declarations

**Conflict of interest** The author(s) declare no conflict of interest with respect to the research, authorship, and/or publication of this article.

**Replication of results** The presented results were mainly obtained using our MATLAB codes and can be provided on reasonable request.

## References


Alexandersen J, Andreasen CS (2020) A review of topology optimisation for fluid-based problems. Fluids 5(1):29

Andreassen E, Clausen A, Schevenels M, Lazarov BS, Sigmund O (2011) Efficient topology optimization in MATLAB using 88 lines of code. Struct Multidisc Optim 43(1):1–16. https://doi.org/10.1007/s00158-010-0594-7

Ardekani AM, Joseph DD, Dunn-Rankin D, Rangel RH (2009) Particle-wall collision in a viscoelastic fluid. J Fluid Mech 633:475–483. https://doi.org/10.1017/S0022112009990632

Andreasen CS (2020) A framework for topology optimization of inertial microfluidic particle manipulators. Struct Multidisc Optim 61(6):2481–2499. https://doi.org/10.1007/s00158-019-02483-5

Ardekani AM, Rangel RH (2008) Numerical investigation of particle–particle and particle–wall collisions in a viscous fluid. J Fluid Mech 596:437–466. https://doi.org/10.1017/S0022112007009688

Bendsøe MP, Kikuchi N (1988) Generating optimal topologies in structural design using a homogenization method. Comput Methods Appl Mech Eng 71(2):197–224. https://doi.org/10.1016/0045-7825(88)90086-2

Balevičius R, Kačianauskas R, Mroz Z, Sielamowicz I (2006) Discrete element method applied to multiobjective optimization of discharge flow parameters in hoppers. Struct Multidisc Optim 31(3):163–175. https://doi.org/10.1007/s00158-005-0596-z

Borrvall T, Petersson J (2003) Topology optimization of fluids in Stokes flow. Int J Numer Methods Fluids 41(1):77–107. https://doi.org/10.1002/fld.426

Craveiro MV, Gay Neto A, Wriggers P (2021) Contact between rigid convex NURBS particles based on computer graphics concepts. Comput Methods Appl Mech Eng 386:114097. https://doi.org/10.1016/j.cma.2021.114097

Cheon Y-J, Kim H-G (2018) An efficient contact algorithm for the interaction of material particles with finite elements. Comput Methods Appl Mech Eng 335:631–659. https://doi.org/10.1016/j.cma.2018.02.005

Campbell J, Vignjevic R, Libersky L (2000) A contact algorithm for smoothed particle hydrodynamics. Comput Methods Appl Mech Eng 184(1):49–65

Chen Z, Wang G, Xue D, Bi Q (2020) Simulation and optimization of gyratory crusher performance based on the discrete element method. Powder Technol 376:93–103. https://doi.org/10.1016/j.powtec.2020.07.034

Choi YH, Yoon GH (2023a) A MATLAB topology optimization code to control the trajectory of particle in fluid. Struct Multidisc Optim 66(4):91. https://doi.org/10.1007/s00158-023-03538-4

Choi YH, Yoon GH (2023b) Particle-structure collision modeling for topology optimization. J Comput Struct Eng Inst Korea 36(6):365–370. https://doi.org/10.7734/COSEIK.2023.36.6.365

Choi YH, Yoon GH (2024) A new density filter for pipes for fluid topology optimization. J Fluid Mech 986:9. https://doi.org/10.1017/jfm.2024.170

Dilgen CB, Dilgen SB, Fuhrman DR, Sigmund O, Lazarov BS (2018) Topology optimization of turbulent flows. Comput Methods Appl Mech Eng 331:363–393. https://doi.org/10.1016/j.cma.2017.11.029

Deng Y, Liu Z, Wu Y (2017) Topology optimization of capillary, two-phase flow problems. Commun Comput Phys 22(5):1413–1438. https://doi.org/10.4208/cicp.OA-2017-0003

Gui N, Yang X, Tu J, Jiang S (2016) A generalized particle-to-wall collision model for non-spherical rigid particles. Adv Powder Technol 27(1):154–163. https://doi.org/10.1016/j.apt.2015.12.002

Joseph GG, Zenit R, Hunt ML, Rosenwinkel AM (2001) Particle-wall collisions in a viscous fluid. J Fluid Mech 433:329–346. https://doi.org/10.1017/S0022112001003470

Kildashti K, Dong K, Samali B (2020) An accurate geometric contact force model for super-quadric particles. Comput Methods Appl Mech Eng 360:112774. https://doi.org/10.1016/j.cma.2019.112774

Lundgaard C, Alexandersen J, Zhou M, Andreasen CS, Sigmund O (2018) Revisiting density-based topology optimization for fluid–structure-interaction problems. Struct Multidisc Optim 58(3):969–995. https://doi.org/10.1007/s00158-018-1940-4

Matuttis H-G, Chen J (2014) Understanding the discrete element method: simulation of non-spherical particles for granular and multi-body systems. Wiley

Meyer CJ, Deglon DA (2011) Particle collision modeling—a review. Miner Eng 24(8):719–730. https://doi.org/10.1016/j.mineng.2011.03.015

Masoero E, O'Shaughnessy C, Gosling PD, Chiaia BM (2022) Topology optimization using the discrete element method. Part 2: material nonlinearity. Meccanica 57(6):1233–1250. https://doi.org/10.1007/s11012-022-01492-x

O'Regan S, Frawley PJ, Shardt O (2023) The effects of particle shape, orientation, and Reynolds number on particle-wall collisions. Comput Fluids 266:106053. https://doi.org/10.1016/j.compfluid.2023.106053

O'Shaughnessy C, Masoero E, Gosling PD (2022) Topology optimization using the discrete element method. Part 1: methodology, validation, and geometric nonlinearity. Meccanica 57(6):1213–1231. https://doi.org/10.1007/s11012-022-01493-w

Peng Z, Doroodchi E, Moghtaderi B (2020) Heat transfer modelling in discrete element method (DEM)-based simulations of thermal processes: theory and model development. Prog Energy Combust Sci 79:100847. https://doi.org/10.1016/j.pecs.2020.100847

Papoutsis-Kiachagias E, Kontoleontos E, Zymaris A, Papadimitriou D, Giannakoglou K (2011) Constrained topology optimization for laminar and turbulent flows, including heat transfer. In: CIRA (ed) EUROGEN, evolutionary and deterministic methods for design, optimization and control, Capua, Italy

Paulick M, Morgeneyer M, Kwade A (2015) Review on the influence of elastic particle properties on dem simulation results. Powder Technol 283:66–76. https://doi.org/10.1016/j.powtec.2015.03.040

Popp A (2018) State-of-the-art computational methods for finite deformation contact modeling of solids and structures. Springer, Cham, pp 1–86. https://doi.org/10.1007/978-3-319-90155-8_1

Sommerfeld M, Huber N (1999) Experimental analysis and modelling of particle-wall collisions. Int J Multiph Flow 25(6):1457–1489. https://doi.org/10.1016/S0301-9322(99)00047-6

Sigmund O, Maute K (2013) Topology optimization approaches. Struct Multidisc Optim 48(6):1031–1055. https://doi.org/10.1007/s00158-013-0978-6

Sommerfeld M (2003) Analysis of collision effects for turbulent gas-particle flow in a horizontal channel: part I. Particle transport. Int J Multiph Flow 29(4):675–699. https://doi.org/10.1016/S0301-9322(03)00031-4

Svanberg K (1987) The method of moving asymptotes-a new method for structural optimization. Int J Numer Methods Eng 24(2):359–373

Tavarez FA, Plesha ME (2007) Discrete element method for modelling solid and particulate materials. Int J Numer Methods Eng 70(4):379–404. https://doi.org/10.1002/nme.1881

van Dijk NP, Maute K, Langelaar M, Keulen F (2013) Level-set methods for structural topology optimization: a review. Struct Multidisc Optim 48(3):437–472. https://doi.org/10.1007/s00158-013-0912-y

Wang J, Zhang M, Feng L, Yang H, Wu Y, Yue G (2020) The behaviors of particle-wall collision for non-spherical particles: experimental investigation. Powder Technol 363:187–194. https://doi.org/10.1016/j.powtec.2019.12.041

Yoon GH, Kim YY (2003) The role of s-shape mapping functions in the simp approach for topology optimization. KSME Int J 17(10):1496–1506. https://doi.org/10.1007/BF02982329

Yoon GH (2010) Topology optimization for stationary fluid–structure interaction problems using a new monolithic formulation. Int J Numer Methods Eng 82(5):591–616. https://doi.org/10.1002/nme.2777

Yoon GH, Kim MK (2023) Topology optimization for transient two-phase fluid systems with continuous behavior. Finite Elem Anal Des 225:104017. https://doi.org/10.1016/j.finel.2023.104017

Yoon GH (2020) Transient sensitivity analysis and topology optimization for particle motion in steady state laminar fluid. Comput Methods Appl Mech Eng 367:113096. https://doi.org/10.1016/j.cma.2020.113096

Yoon GH (2022) Transient sensitivity analysis and topology optimization of particle suspended in transient laminar fluid. Comput Methods Appl Mech Eng 393:114696. https://doi.org/10.1016/j.cma.2022.114696

Zhou M, Lazarov BS, Wang F, Sigmund O (2015) Minimum length scale in topology optimization by geometric constraints. Comput Methods Appl Mech Eng 293:266–282. https://doi.org/10.1016/j.cma.2015.05.003

Zhu HP, Zhou ZY, Yang RY, Yu AB (2008) Discrete particle simulation of particulate systems: a review of major applications and findings. Chem Eng Sci 63(23):5728–5770. https://doi.org/10.1016/j.ces.2008.08.006